Double-sided Metrology of 2S Modules for the CMS Phase-2 Tracker Upgrade: Preparations for Serial Production and Measurements at Operating Temperature

von

Patrick Juraschitz

Masterarbeit in Physik

vorgelegt der
Fakultät für Mathematik, Informatik und Naturwissenschaften
der
Rheinisch-Westfälischen Technischen Hochschule Aachen

im August 2022

angefertigt im

I. Physikalischen Institut (IB)

bei

Professor Dr. Lutz Feld

Zweitgutachter

Professor Dr. Oliver Pooth

Contents

1 Introduction

Physicists use particle accelerator experiments to study the interactions of elementary particles. Therefore, particle beams with high energy are required. The first actual particle accelerator was built 90 years ago by Cockroft, Walton and Rutherford. The machine was capable of producing a collimated beam with an energy of 400 keV [1]. Since then, accelerators have been greatly improved and built in several types: synchrotrons, cyclotrons, and linear accelerators. The Large Hadron Collider (LHC) [2] is to date the most powerful particle accelerator and can produce proton beams with energies up to 6.8 TeV, which is ten million times more powerful than the 1932 accelerator.

The LHC was built to study the Standard Model (SM) of particle physics. The SM is a theory that describes the constituents of matter and the interactions between them at the most fundamental level to date. When particles, primarily protons, collide in the LHC with sufficient energy, new particles are created. Detector experiments such as the Compact Muon Solenoid (CMS)[3] at the LHC can measure particles and are built to compare theoretical SM production rates with real data. Physicists look for deviations of actual data from SM predictions to gain insight into possible theories beyond the SM, which must exist because the SM is known to be incomplete. For example, it does not include gravity and cannot explain the origin of dark matter. Rare processes are often the most promising when looking for such deviations.

To increase the potential of the LHC to produce rare events, the luminosity of the LHC will be increased during the planned High Luminosity LHC (HL-LHC) upgrade [4]. Consequently, the CMS experiment also needs to be improved with the Phase-2 upgrade. Part of the upgrade involves an entirely new tracking system of CMS [5]. The detector modules of the so-called Outer Tracker will consist of two closely spaced planar silicon sensors that are read out by the same readout electronics.

This work deals with precision measurements of one type of the new modules, called 2S modules, which must meet specific precision requirements to function correctly. The Double-sided Metrology (DSM) machine is a setup in Aachen, designed for sensor-to-sensor alignment measurements of 2S modules, and is used for all measurements in this work. After a brief introduction to the LHC and the CMS experiment, the setup, measurements, and software used to control the setup will be explained. An analysis of the statistical and systematic uncertainties of the measured sensor-to-sensor alignment is presented afterwards. General improvements to the setup were introduced during the course of this work that are aimed at improving the ease of use and increasing the measurement speed. The setup has been improved to allow measurements at temperatures as low as $-10°C$. The development of the improved setup is described in the next chapter. Then, sensor-to-sensor alignment results of various modules are shown, including measurements between $+35°C$ and $-10°C$. Finally, a new measurement method and initial results are presented to measure the alignment of sensors to the supporting structure of the 2S module.

2 The LHC, the CMS Experiment and the 2S Module

The LHC collides protons to obtain information about the SM and to gain insight into theories beyond. Due to the rarity of interesting processes, a high number of collisions have to be provided. The number of collisions per surface area and per time is described by a parameter called luminosity, L. The LHC was originally designed for an instantaneous luminosity of $L = 1.0 \cdot 10^{34}\,\mathrm{cm^{-2}s^{-1}}$ [2]. The collider has already reached twice this original design value due to several upgrades performed in the past. The biggest upgrade, the high luminosity LHC (HL-LHC) upgrade, is supposed to increase the luminosity to $5.0 - 7.5 \cdot 10^{34}\,\mathrm{cm^{-2}s^{-1}}$ [4].
As important as the generation of rare particles is their detection. Various detector experiments are built. The CMS experiment is one of the two general-purpose detectors at the LHC. The CMS experiment will also be upgraded in conjunction with the HL-LHC upgrade. Two main challenges must be faced in the CMS Phase-2 Tracker Upgrade due to the increased luminosity of the HL-LHC: improving the detector so it can withstand the higher radiation and coping with the increased data rates.
The experimental setup of the LHC and the CMS experiment is presented in the following. In addition, the main technical improvements of the HL-LHC and the CMS Phase-2 Tacker Upgrade are also highlighted.

2.1 The Large Hadron Collider

The Large Hadron Collider is located below the France-Switzerland border near Geneva, operated by the European Organization for Nuclear Research (CERN) [2]. It is a synchrotron accelerator built in the tunnel of the former Large Electron Positron Collider and has a circumference of 26.7 km. The LHC accelerates protons and heavy ions in opposite directions in separate tubes. Colliding protons reach center of mass energies, $\sqrt{s}$, of up to 13.6 TeV [6]. Superconducting NbTi magnets generate a field of 8.3 T, operated at temperatures below 2 K. The magnets force the particles on their circular trajectory. The required magnetic field is proportional to the particle energy. Before they are injected into the LHC tunnel, it is necessary to pre-accelerate the particles. Therefore, particles pass through four pre-accelerators: the linear accelerator LINAC4 (here, negative hydrogen atoms are accelerated, and their electrons are subsequently removed), the Proton Synchrotron Booster (PSB), the Proton Synchrotron (PS), and finally the Super Proton Synchrotron (SPS), shown in Figure 2.1. The proton energies after each segment are summarized in Table 2.1.

The particles are filled into the LHC in 2808 bunches per beam, whereas each bunch contains roughly 10^{11} protons. Between each bunch, there is a spacing of 25 ns. The number of interactions per bunch crossing is called pileup. In the LHC, particles are accelerated by radiofrequency cavities, which generate an altering electromagnetic field to finally increase the proton energy up to 6.8 TeV.
The beam pipes cross each other at four interaction points corresponding to the locations of the four main detector experiments (Figure 2.1). A Large Ion Collider Experiment (ALICE)

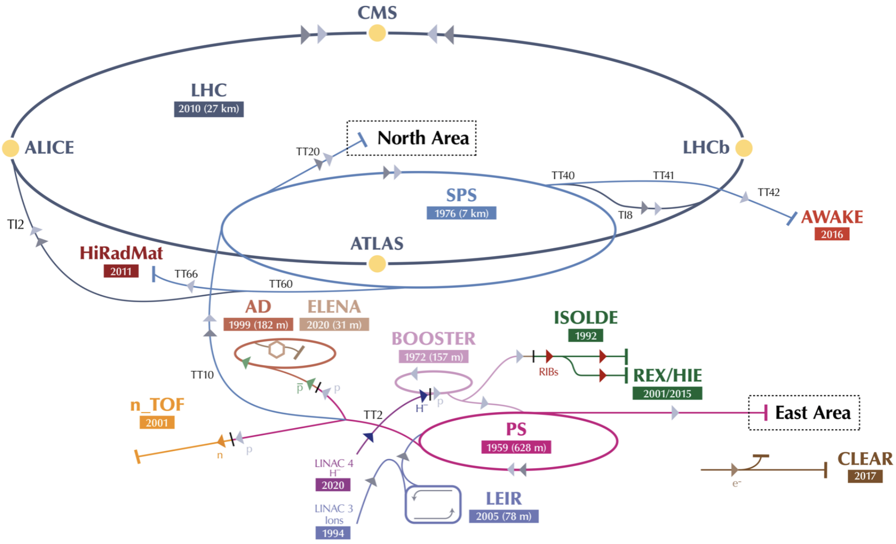

Figure 2.1: A scheme of the CERN accelerator complex [7].

Accelerator	Energy
Linear Accelerator 4	160 MeV
Proton Synchrotron Booster	2 GeV
Proton Synchrotron	26 GeV
Super Proton Synchrotron	450 GeV

Table 2.1: Maximum particle energy after each acceleration stage at the CERN accelerator complex [7].

studies heavy-ion collisions and the Large Hadron Collider beauty (LHCb) focuses on b-quark physics. A toroidal LHC apparatus (ATLAS) and CMS are multipurpose detectors that study different areas of particle physics and use complementary methods.

2.1.1 The High Luminosity LHC Upgrade

The (instantaneous) luminosity is defined as the ratio of the number of interactions per time interval to the cross section. The integrated luminosity is a direct measure of the total number of produced events over a period of time. During so-called long shutdowns (LS), the LHC machine is upgraded. One primary interest of these upgrades is to increase the luminosity of LHC to increase the absolute number of rare events.
The LHC started taking data from 2010 to 2012 (Run 1) with a maximal luminosity of $0.77 \cdot 10^{34}\mathrm{cm}^{-2}\mathrm{s}^{-1}$ and delivered an integrated luminosity of $30\,\mathrm{fb}^{-1}$ [8]. These values increased to $2.1 \cdot 10^{34}\,\mathrm{cm}^{-2}\mathrm{s}^{-1}$ and $193\,\mathrm{fb}^{-1}$ in Run 2 after improvements made during Long Shutdown 1 (LS1). Run 3 has just started and will go on until 2025 with a planned peak luminosity of $2.0 \cdot 10^{34}\,\mathrm{cm}^{-2}\mathrm{s}^{-1}$ to reach an integrated luminosity of $350\,\mathrm{fb}^{-1}$. After that, from 2026 to 2028, the LHC will be shut down for its biggest upgrade, the HL-LHC upgrade. This upgrade is supposed to enhance the luminosity to $5.0 - 7.5 \cdot 10^{34}\,\mathrm{cm}^{-2}\mathrm{s}^{-1}$. The HL-LHC is expected to

achieve an integrated luminosity of $3000 - 4000\,\mathrm{fb}^{-1}$.
For the upgrade, several parts will be improved, e.g. the inner quadrupole magnets, the collimation system, and the RF cavities [9].

2.2 The Compact Muon Solenoid Experiment

The research program of CMS covers different fields. The main goals are to study the Higgs-Boson, search for supersymmetry, and study heavy ion collisions. Its biggest achievement was the discovery of the Higgs-Boson in 2012 [10]. The detector is placed at intersection point 5, near the village Cessy in France. The name of the experiment already highlights some key aspects:

- Compact: The detector is built compact. It is arranged in a cylindrical shape with a length of 21 m and a diameter of 15 m with a weight of 14000 t.
- Muon: CMS is good at measuring muon tracks.
- Solenoid: The special feature of the experiment is a solenoid magnet that generates a magnetic field of 3.8 T and bends the paths of charged particles.

CMS uses a right-handed coordinate system with the origin corresponding to the interaction point. The z-axis points along the beam axis, the x-axis points towards the center of the LHC, and the y-axis points upwards. The directional parameters computed from the detector information are the azimuthal angle ϕ in the x-y plane and the so-called pseudo-rapidity η. The pseudo-rapidity is an implicit measure of the polar angle θ, which is the angle between a track of a particle and the z-axis. The pseudo-rapidity is defined as:

$$\eta = -\ln\left(\tan\frac{\theta}{2}\right). \tag{2.1}$$

The radial distance to the z-axis is denoted as r.
A cutaway view of the detector with its technical data is shown in Figure 2.2. Layers of different subdetectors built around the beam tube form the entire detector. In the following, these subdetector systems will be explained from inner to outer.

Silicon Pixel Detector

The Phase-1 Pixel Detector directly surrounds the beam pipe [12]. It detects tracks of charged particles and their origin with high precision. The system consists of about 1800 modules arranged in layers, four in the barrel region and three in the endcaps. Each module contains about 66000 pixels with a size of $100 \times 150\,\mu\mathrm{m}^2$. The detection principle is based on a silicon semiconductor with a depletion zone operated with high voltage in the reverse bias mode. A charged particle passing through the sensor creates electron-hole pairs that generate a measurable electrical signal in a pixel. The layers of modules, the first of which is only 2.9 cm away from the beam pipe, create three-dimensional information about the trajectory

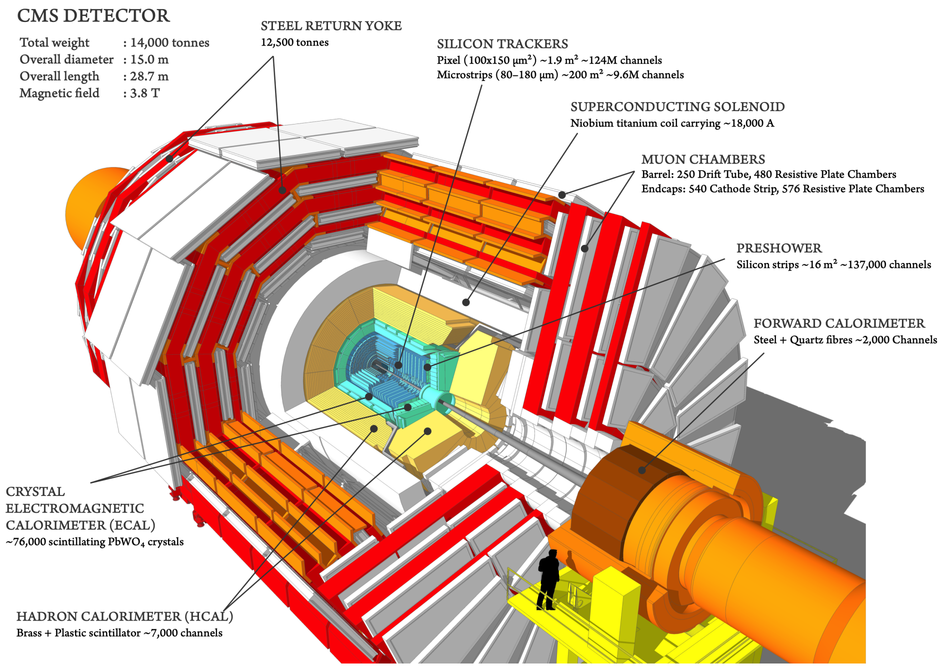

Figure 2.2: A sketch of the CMS detector. The relation to a human illustrates its size [11].

of charged particles by combining the two-dimensional hit positions. The primary vertex position reconstruction of a particle can be determined with a precision of about 10 μm in all spacial directions [13]. Due to its location being so close to the interaction point, this subdetector suffers the most from radiation damage. To minimize this damage, the pixel detector is kept at a temperature of about −20 °C.

Silicon Strip Detector

A total of 15200 strip modules, installed in ten layers, surround the pixel detector. These layers are further divided into four regions: the Tracker Inner Barrel (TIB), the Tracker Inner Disks (TID), the Tracker Outer Barrel (TOB), and the Tracker Endcaps (TEC). The outermost layer is placed at a radius of nearly 1.1 m. The detection principle is similar to the pixel detector, but in contrast, the strip detector measures hits in the one-dimensional strips. In total, 10 million strips measure hits of particles. The radiation in this region is still high, which is why it is also kept at −20 °C.

Electromagnetic calorimeter (ECAL)

The ECAL measures the energy of electromagnetically interacting particles, such as electrons and photons. It consists of lead tungstate crystals that scintillate when a particle passes through them. The light from the scintillation is proportional to the energy of the particle deposited in the ECAL. There are 75848 crystals, each weights about 1.5 kg. The ECAL reaches out to a radius of 1.7 m.

Hadronic calorimeter (HCAL)

The HCAL is used to measure the energy of hadrons, for example neutrons, which penetrate the ECAL without much disturbance. The HCAL reaches from a radius of 1.8 m to 2.9 m. It is built as a so-called sampling calorimeter, meaning it consists of alternating layers of absorber and detector material. Hadrons interact inelastically with brass plates, generating hadronic showers made of charged particles and photons. These showers can then be detected from plastic scintillators that produce rapid light pulses.

Solenoid magnet

The magnet is used to bend the trajectory of charged particles. The charge of a particle can be inferred from the direction in which the particle is bent. Oppositely charged particles turn in opposite directions. Additionally, one can measure the momentum of charged particles. Due to the Lorentz force, particles with higher momentum are bent less than particles with lower momentum. The solenoid is made of superconducting NbTi, generating a magnetic field of up to 3.8 T. It has a diameter of 6 m. Three layers of iron (that also enclose the muon chambers) surround the magnet and guide the magnetic field. The outermost steel return yoke has a diameter of 14 m. The magnet and yokes also act as a filter, letting through only muons and exclusively weakly interacting particles such as neutrinos. With a weight of 12500 t the magnet is by far the heaviest piece of the CMS experiment.

Muon chambers

Muons interact very rarely, which is why they can penetrate all other layers of the CMS experiment. The detection of muons is essential because they are produced in many decays. For instance, the tau lepton and the b-quark were discovered via their decays to muons. Because of their clean signal, muons are also used for the trigger system of CMS [14]. The muon chambers are filled with gas. When a muon passes through, it ionizes gas particles, which can be measured. Four layers of chambers are interleaved with the return yokes. In total, there are 1400 muon chambers. To track the muons, 250 drift tubes (DTs) and 540 cathode strip chambers (CSCs) are used. In addition, 610 resistive plate chambers (RPCs) form a trigger system. The outermost muon chamber also builds the very last layer of the CMS experiment and surrounds the whole detector at a diameter of 15 m.

At the design luminosity of $L = 1.0 \cdot 10^{34}\,\text{cm}^{-2}\text{s}^{-1}$, the LHC produces roughly 1 billion proton-proton interactions per second. With modern techniques, it is impossible to build enough storage to save the data of all collisions. The most interesting events are those corresponding to particles with high transverse momentum. About 95 % of the particles have a transverse momentum of $p_T < 2\,\text{GeV}$. Therefore, it is useful to build a trigger system and store only a fraction of all data. CMS uses a two-stage trigger system. The first is a hardware trigger (L1 trigger), with an output rate of 100 kHz. It decides which events to read out based on momentum thresholds. The second stage is the high level software trigger (HLT), which analyses the previously temporally stored data more carefully and decides which events are stored permanently at a rate of 1 kHz.

2.3 The CMS Phase-2 Tracker Upgrade

The HL-LHC will provide a luminosity of $5.0 - 7.5 \cdot 10^{34}\,\text{cm}^{-2}\text{s}^{-1}$ with a pileup of $140 - 200$ [4]. This environment presents two major challenges: the parts must withstand the high levels of radiation damage and process the increased amount of data. Several parts of the detector will be upgraded from the muon system to the innermost tracker. This thesis contributes to the Outer Tracker of the Phase-2 Tracker Upgrade, which is presented in the following. The tracking system of CMS will be subdivided into two parts: the Inner Tracker and the Outer Tracker (Figure 2.3).

The new Inner Tracker replaces the Silicon Pixel Detector. It is longer than the old pixel detector to increase the geometrical coverage to $|\eta| \sim 4$. Being so close to the beam pipe, the tracker has to resist highest hadron fluences of up to $2.3 \cdot 10^{16}\text{n}_{\text{eq}}/\text{cm}^2$ for $3000\,\text{fb}^{-1}$ [5]. Therefore, the design foresees the possibility to exchange degraded parts. Also, the granularity of the detector will be increased to limit the occupancy to the permille level. Additionally, this improves the ability to separate tracks.

The Outer Tracker is subdivided into different parts, as shown in Figure 2.3b. Modules are installed between $r \approx 21\,\text{cm}$ and $r \approx 112\,\text{cm}$. The Barrel region is split into two parts, containing different module types: the PS module and the 2S module. A PS module contains a strip and a macro-pixel sensor, and a 2S module is built from two strip sensors. Both types of modules contain a gap between the sensors to take advantage of the p_T module concept described at the end of this section. The Tracker Barrel is populated with PS modules (TBPS) and the Tracker Barrel with 2S modules (TB2S), the latter type being explained in greater detail in Section 2.3.1. Both PS and 2S modules are mounted in the Tracker Endcap Double-Discs (TEDD). In the TBPS 2872 PS modules are increasingly tilted with increasing z so that particles emerging from the interaction point are more likely to hit the modules perpendicular to the surface. In this region, hadron fluences can still be as high as $9.6 \cdot 10^{14}\text{n}_{\text{eq}}/\text{cm}^2$ [5]. The TB2S ensembles 4464 2S modules, mounted on ladder structures and stacked in three layers with the module surface parallel to the z-axis. In the TEDD, a total of 5960 (2744 PS and 3216 2S) modules are installed with the surface of the modules perpendicular to the z-axis. The arrangement is chosen such that nearly every particle with $|\eta| < 2.4$ produces hits in at least six layers of modules. This way, a sufficiently robust tracking performance of the Outer Tracker can be ensured, which is needed for the L1 Trigger.

The inclusion of the Outer Tracker data to the L1 trigger system is one of the biggest goals for the CMS Phase-2 Tracker Upgrade. The Outer Tracker is supposed to reject particles with $p_T < 2\,\text{GeV}$. This reduces the data by a factor of 10 to 100, depending on module location [5]. Therefore, the whole system uses a new module concept, presented in the following.

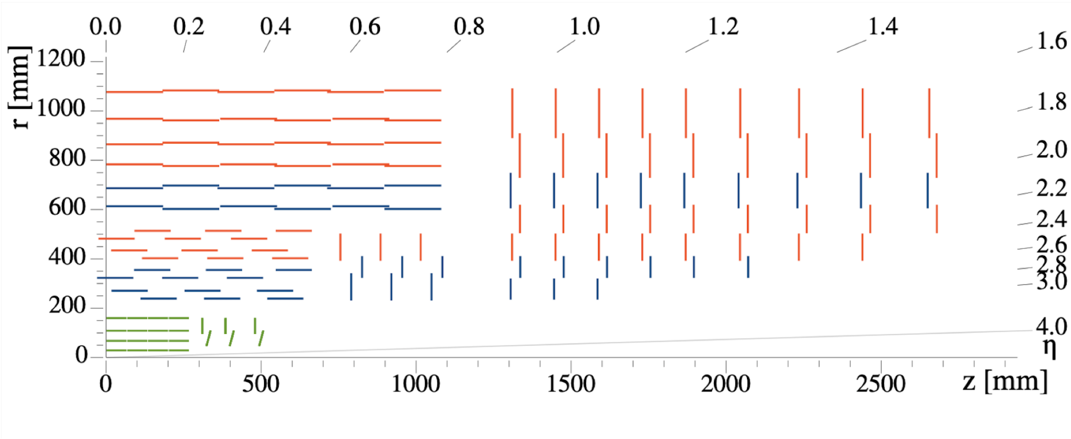

(a) The CMS Phase-1 Tracker: the pixel detector is illustrated by the green lines, and the strip detector is indicated as red and blue lines. Red lines refer to single-sided modules, while blue lines refer to double-sided modules [5].

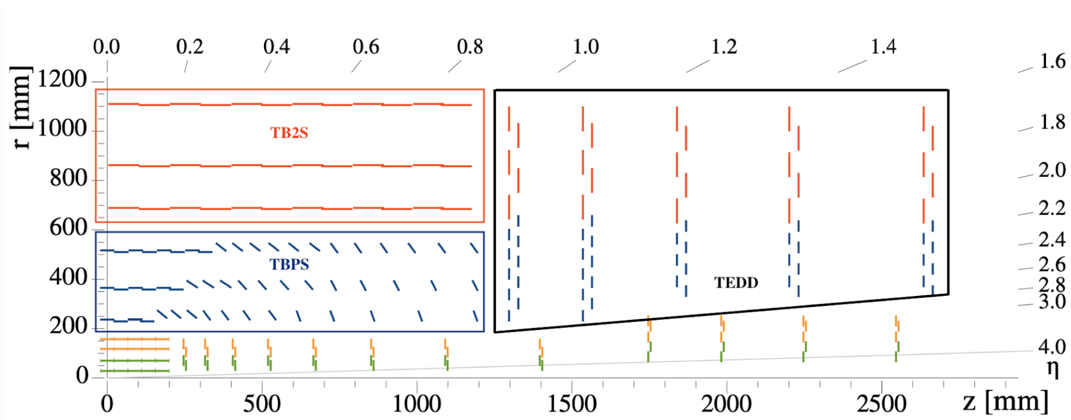

(b) The CMS Phase-2 Tracker: The Inner Tracker is shown in orange and green, while the Outer Tracker and its further sub-areas are shown in red and blue. Modified from Ref. [5].

Figure 2.3: Sketches of one quarter of the CMS tracker before (top) and after (bottom) the Phase-2 Upgrade. Different colors indicate different module types.

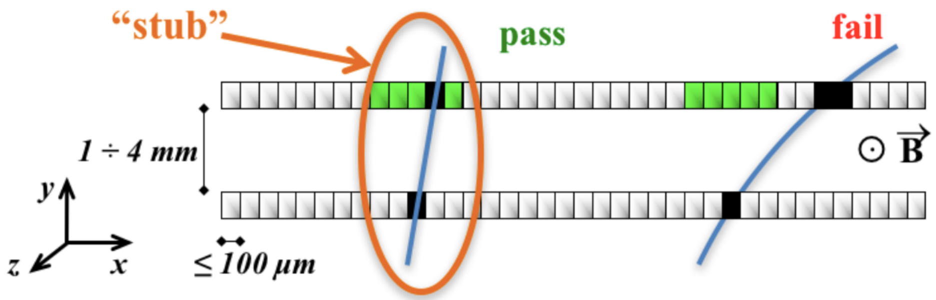

Figure 2.4: A schematic view of a p_T module. Each individual box represents a strip of the upper and the lower sensor, while a black box indicates a hit in a particular strip. The green boxes show the channels that define the window the particle must hit to be accepted as a stub. Example particle tracks with sufficient momentum (left) and too little momentum (right) are shown in blue [5].

The p_T module

The p_T module design uses the bending power of the strong solenoid of the CMS experiment within every individual module.
The curvature of the track of a charged particle in the magnetic field can be used as a measure of the momentum of the particle, according to:

$$p_T = q \cdot R \cdot B, \tag{2.2}$$

where q is the charge of the particle, R is the bending radius, and B is the magnetic field. Since p_T is by definition the portion of the momentum pointing perpendicular to the beam tube, it points perpendicular to the direction of the B field. The equation follows from the equality of the Lorentz force and the centrifugal force. Given $p_T \sim R$, particles with lower momentum are deflected more than particles with higher momentum.
If each p_T module consists of two sensors with a small gap between them (Figure 2.4), one can derive an estimate of the particle momentum by comparing the hit position in the lower sensor with the hit position in the upper sensor. Only when the measured location falls within a specific interval around the location in the lower sensor does the module send a so-called "stub" signal. If a particle hits outside the interval, it means that the particle's momentum is too low. The interval is chosen according to the desired threshold. Both PS and 2S modules are built with the new concept.

2.3.1 The 2S Module

A schematic view of a 2S module is depicted in Figure 2.5. The upper and lower n-in-p doped silicon sensors are the key components of a 2S module as they play the role of the sensing device of the CMS Outer Tracker. The about 10 x 10 cm^2 big surface of each sensor consists of 2 x 1016 strips with a length of 5 cm and a distance of 90 μm between the strips, resulting in 2032 individual readout channels. The semiconductor-based detection is fast and well suited

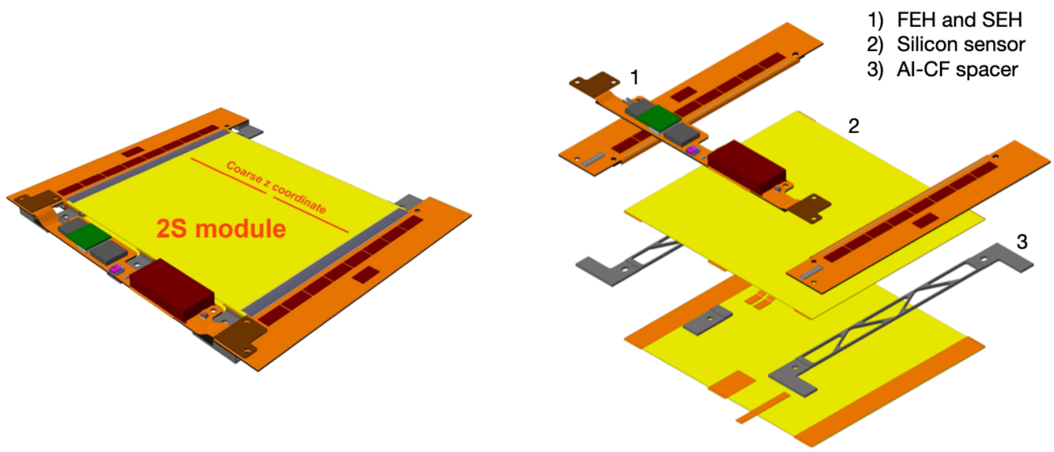

Figure 2.5: CAD drawings of an assembled (left) 2S module and an exploded view (right). In the exploded view, its main components are highlighted. Modified from Ref. [5].

for the detection at the high frequency of bunch crossings and the use for the L1 trigger.
The sensors are glued to aluminum carbon fibre spacers that ensure a gap of 1.8 mm or 4 mm between the sensors. The material has a low coefficient of thermal expansion (3 ppm/°C [5]), which is matched to the coefficient of the sensor (4 ppm/°C [5]). This ensures a stable precision of the module at low temperatures. The modules are mounted on the cooling structure in the experiment via the holes in the spacers. Two additional Al-CF pieces with holes are glued halfway along the strips on both sides between the sensors, serving as additional mounting and, more important additional cooling contacts. The spacers are fixed on pins that are connected to cooling tubes. Two-phase CO_2 flowing through the tubes cools down the pins and thus the module.
The acceptance window size of a p_T module increases linearly with the gap size created by the spacer at first order [5]. A larger gap provides better p_T resolution, while the simultaneously increasing acceptance window can catch more random combinations of hits from different particles. Secondarily, the slightly higher material costs resulting from the thicker bridge are also taken into account. The final setup represents a compromise of both gap size effects. Modules with a 1.8 mm gap are installed in regions with higher particle flux. In the outer areas, fewer random particle combinations occur so that one can take advantage of the better resolution of the 4 mm modules.
The signals are processed by two front end hybrids (FEHs) on both module sides. Each FEH uses eight CMS binary Chips (CBC) [5] to read out the signals from the strips and one concentrator chip to collect, buffer and further transmit the CBC data. Every CBC reads out 127 strips of both sides, resulting in 254 channels per CBC. Each strip is wire-bonded to a readout channel [5]. In addition, every module features one service hybrid (SEH). The SEH merges the data from both FEHs and sends it through a single optical fibre to the back-end. The SEH also has two DC-DC converters that provide $1.25 - 2.55$ V power supply for each module [5].

Module assembly in Aachen

For the CMS Phase-2 Tracker Upgrade, RWTH Aachen will contribute 800 2S modules. The aim is to produce four modules per day, corresponding to an estimate of one year of pure module production. Precision measurements and electrical tests will be performed for each module produced.
According to the current plans, the preproduction phase will last until April 2024, followed by nearly two years of production phase until March 2026. During this period, the various production centers have to assemble 7680 2S modules.

Precision requirements

The stub mechanism relies on accurately comparing the hit positions in both sensors. The window that defines which particles meet the p_T threshold is centered around a straight trajectory of a particle. If the particle passes the lower sensor at an angle, the hit in the upper sensor will not be generated in the same channel number as in the lower sensor. This is due to the fact that the two sensors have a gap and are therefore located at different radii, but the strips of both sensors have the same pitch. The effect is illustrated in Figure 2.6. The stub finding logic can correct such offset, but only with a precision of half a pitch due to the binary readout [5].

A tilt of one sensor with respect to the other introduces a varying offset along the module (Figure 2.7). Such an offset cannot be corrected because different channel combinations would be superimposed at different positions along the width of the module. The tilt t between the sensors must be significantly smaller than half a pitch, which is the limit on the offset correction. To keep the effect of a tilt small, a target of $t < 20\,\mu\text{m}$ is chosen which is about a quarter of the pitch of a 2S module. Since there are two rows of strips, the limit on t has to be doubled when considering the whole module width. With a module width of about 10 cm, this results in a limit on the rotation of $\theta_{tilt} < 400\,\mu\text{rad}$.

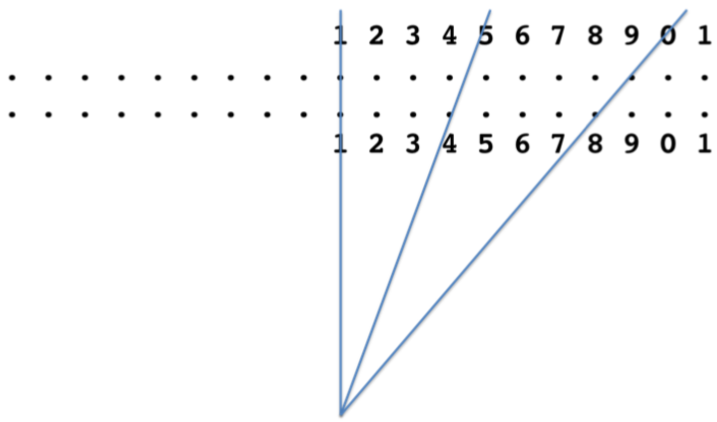

Figure 2.6: The blue lines represent straight trajectories of particles passing a 2S module. It is shown, that straight lines generally do not pass the same channel number of both sensors [5].

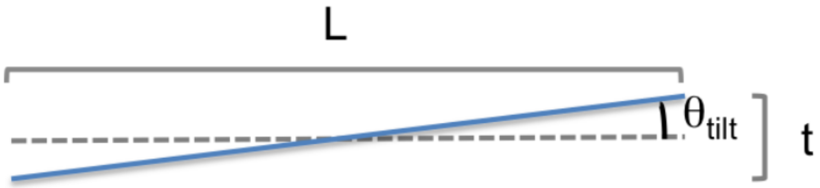

Figure 2.7: An illustration of two sensors tilted with respect to each other. One sensor is shown in blue and one as a dashed line. The modules are tilted by t over the strip length L. The tilt angle between the sensors is denoted as θ_{tilt} [5].

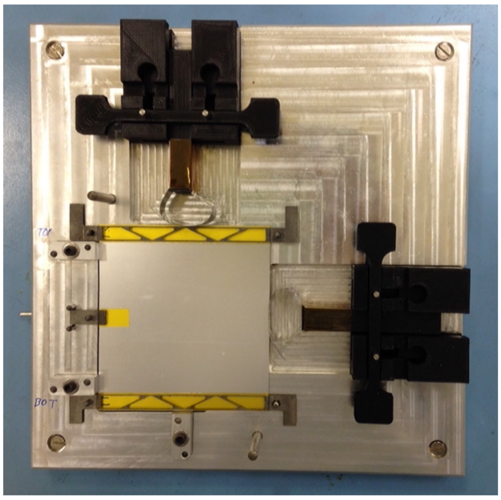

Figure 2.8: A picture of the so-called sensor gluing jig needed to glue the sensors to the Al-CF bridges. The image shows the lower sensor of a 2S bare module that is pushed into three alignment pins by two springs. The holes of the bridges are placed on small pins to keep them in the correct position [5].

Also, preliminary requirements on the translational shifts are set: a shift perpendicular to the strips, Δx, smaller than 50 µm and the shift along the strips, Δy, smaller than 100 µm [5].

Module construction

The sensors and spacers must be assembled with enough precision to meet the previously set requirements. Therefore, the sensors are glued onto the spacers on standardized so-called "sensor gluing jigs" (Figure 2.8). The jig is used to precisely position the sensors with respect to the spacers. For assembly, two springs push the sensor onto three machined precision stops. The spacers are fixed by four small pins and are glued onto the sensor. The second sensor is pushed into the same precision stops to align the edges of both sensors. The assembly precision of this so-called bare module is measured with a metrology system (Section 3).
In subsequent steps, the SEHs and FEHs are glued to the sensor sandwich in a dedicated jig. Wire bonding is then used to establish electrical contact between the sensor and the readout electronics. The wire bonds are encapsulated to prevent loss of contact.

3 The Double-sided Metrology

The Double-sided Metrology (DSM) machine is designed to measure the relative orientation of the two sensors of a 2S module with high precision.
This chapter lays down the basic principle, describes the setup, and explains measurements possible with the DSM machine in the state at the beginning of this work.

3.1 The Basic Principle

To measure the orientation of the sensors with respect to each other, both sides of the module have to be looked at in some way since the sensors are not transparent. Therefore, different methods are used.
Professor Feld proposed the idea of the DSM method. As the name suggests, the setup uses two cameras to look at the module from both sides at the same time. However, this leads to a problem: due to, for example thermal expansion, the field of view in both cameras can never be kept perfectly aligned on a micrometer scale in the long run. Therefore, a common point of reference is needed to compare the images taken by two cameras. This reference point is constructed by rotating the module in the surface plane. The resulting axis of rotation is the common reference point of both cameras (Figure 3.9). To find the axis of rotation, one looks at special alignment markers, which are precisely manufactured at the same position on every sensor. First, the distance from the upper and lower camera to the respective marker, x_{u1} and x_{l1}, is measured. After that, the module is rotated, for example by 180°. The next step is to measure the distance, x_{u2} and x_{l2}, to the markers after the rotation. In this example, the distance of the alignment marker to the rotation axis is then given by the mean of the respective distances to the camera before and after the rotation:

$$r_u = \frac{x_{u1} + x_{u2}}{2} \qquad \text{and} \qquad r_l = \frac{x_{l1} + x_{l2}}{2}.$$

The difference of the radii r_u and r_l is a direct measure of the misalignment, dx, of both sensors:

$$dx = r_u - r_l.$$

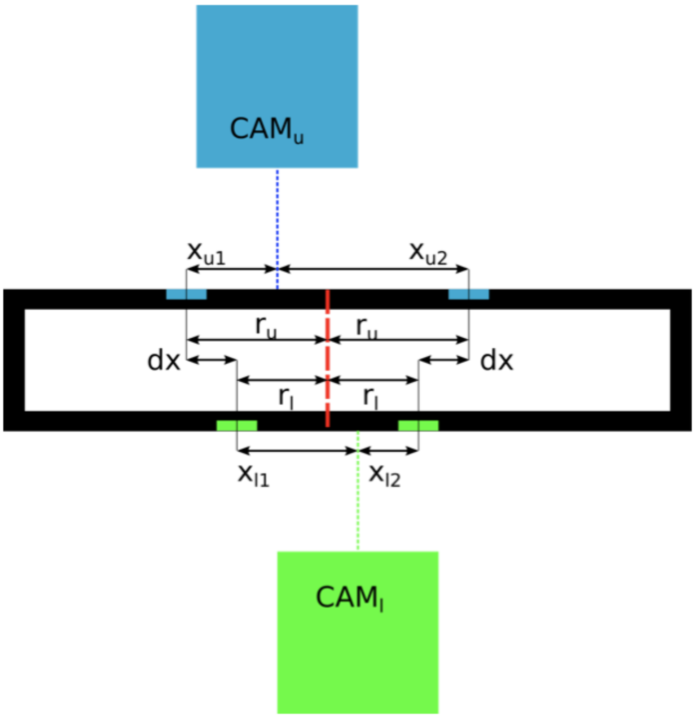

Figure 3.9: A sketch to illustrate the basic principle of the DSM machine. The big blue and green boxes represent the cameras, while the dotted lines are their center of view. The black box illustrates the module. The blue and green misaligned rectangles on the module indicate precision marker positions on the upper and lower sensor and their potential shift with respect to each other before and after a rotation. The rotation axis is shown as a dashed red line. The variables are explained in the text [15].

3.2 The Setup

The complete DSM machine is depicted in Figure 3.10. It was developed by Marius Preuten [15] and further improved by Christian Käseberg [16].
The setup consists of two cameras fixed on axes, a rotation table, and an xy-table with a carbon fiber plate used to fix the module during the measurements. In the following, each component of the setup is presented separately.

The cameras

The cameras of type UI-3250 CP-C-HQ [17] are manufactured by IDS Imaging. They have a resolution of 1600 x 1200 pixels. A microscope lens from Mitutoy (M Plan Apo 10X [18]) creates a sufficiently large image. Coaxial illumination is used, which is ideal for imaging reflective surfaces such as silicon sensors. The depth of field amounts to 15 µm [16]. In the resulting image a pixel has a size of about 0.78 x 0.78 μm^2 resulting in a roughly 1250 x 940 μm^2 big field of view.

The camera axes

The axes of type MPS75SL-100 [19], which allow height adjustments of the cameras, are manufactured by Aerotech. They are specially designed as compact, high-precision linear positioning systems. The minimum incremental motion is 0.1 µm [19], and the axes can move to positions with a precision of 4 µm [16]. The manufacturer has set a limit of 20 mm/s on the velocity.

The xy-table

The xy-table MS-8000 [20] from ASI Imaging is well suited for controlled movements in a plane. To be able to look at the module from the bottom, the table has a hole in the middle. Additionally, an insert can be mounted that can be designed by the user. In the DSM, the insert is a custom-made carbon fibre plate with pins used to fix the module. The plate has a cutout in the center so as not to block the view of the lower camera. The table is controlled by the multi-axes stage controller MS-2000-WK [21] that also allows the use of a joystick. It has an accuracy of ± 3 µm per length of scale [20]. The maximal velocity along each axis is 7.5 mm/s [16].

The rotation table

The rotation table of type APR200DR [22] from Aerotech is used. For the maximum angular velocity, Aerotech set a limit of 30 deg/s. Due to the wiring in the setup, the rotation stage is restricted to movements between $-180°$ and $+200°$. The rotation table and the camera axes use the same control unit; Ensemble MP [23].

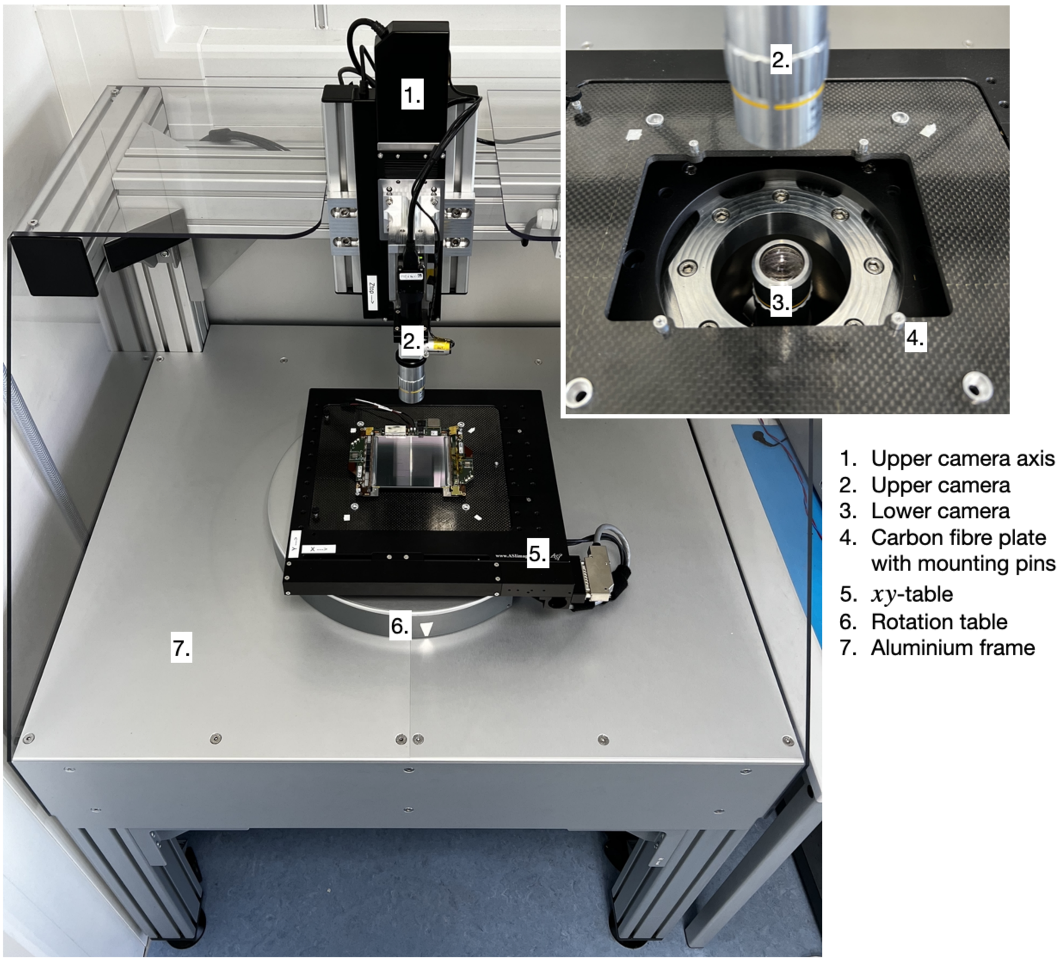

Figure 3.10: A photograph of the DSM setup. The close-up shows both cameras and the carbon fiber plate with the mounting pins. The individual components are numbered.

The described parts are assembled so that the xy-table is attached to the turntable and the axis of rotation is perpendicular to the xy-plane. The carbon fibre plate is fixed in the xy-table by springs and can be adjusted in height with three screws. The assembled camera parts are mounted onto the camera axes. One axis is installed above the xy-table and one below, such that a module lying on the pins of the carbon fibre plate can be seen from both sides. The lower camera looks through the hole of the xy-table. The camera axes move the cameras in the z direction, which ideally coincides with the rotation axes and is perpendicular to the surface of a module mounted on the carbon fiber plate pins. Optionally, a module can be further fixed by additional screwing it on the mounting pins. Unless otherwise stated, all measurements presented in this work were performed without this option, as it does not improve measurement accuracy significantly. The field of view of the cameras can be adjusted to align the center of the picture with the axis of rotation.
This core assembly is placed in a massive aluminum frame that holds the components in place. The entire setup is located in a clean room for measurements in an environment that minimizes the chance of damaging the sensors during serial production.

3.3 The Graphical User Interface

The DSM can be controlled via a graphical user interface (GUI). A screenshot of the GUI, as it was at the start of this thesis, is shown in Figure 3.11. It is separated into three parts: a live image of the two cameras, the manual axes controls, and the module and measurement routines, all further described in the following.

The live camera images

A live picture of both cameras is displayed on the left side of the GUI (Figure 3.11 in green). The upper screen shows the upper camera, while the lower screen shows the lower camera. A red cross in both windows indicates the center of the picture. The live image can be used to confirm that the cameras show what they are supposed to show or to check the sharpness of the picture at certain heights. One can also supervise the machine during measurements to look for problems concerning the image.

The manual axis controls

The manual axis controls (Figure 3.11 in red) allow the user to direct each stage individually. "Top" and "Bottom" refers to the cameras and their axis. "Central" includes the xy-table and the rotation stage. Every stage can be enabled or disabled with the corresponding buttons. For a stage to be able to move, it must first be enabled. Positions can be entered with a step size of 1 µm in case of the camera axes and the xy-table and $0.01°$ for the rotation stage. The cameras can also vary the brightness by entering values between 0 and 255 (8 bit). Each live value or position where an enabled stage is located is also displayed and constantly updated.

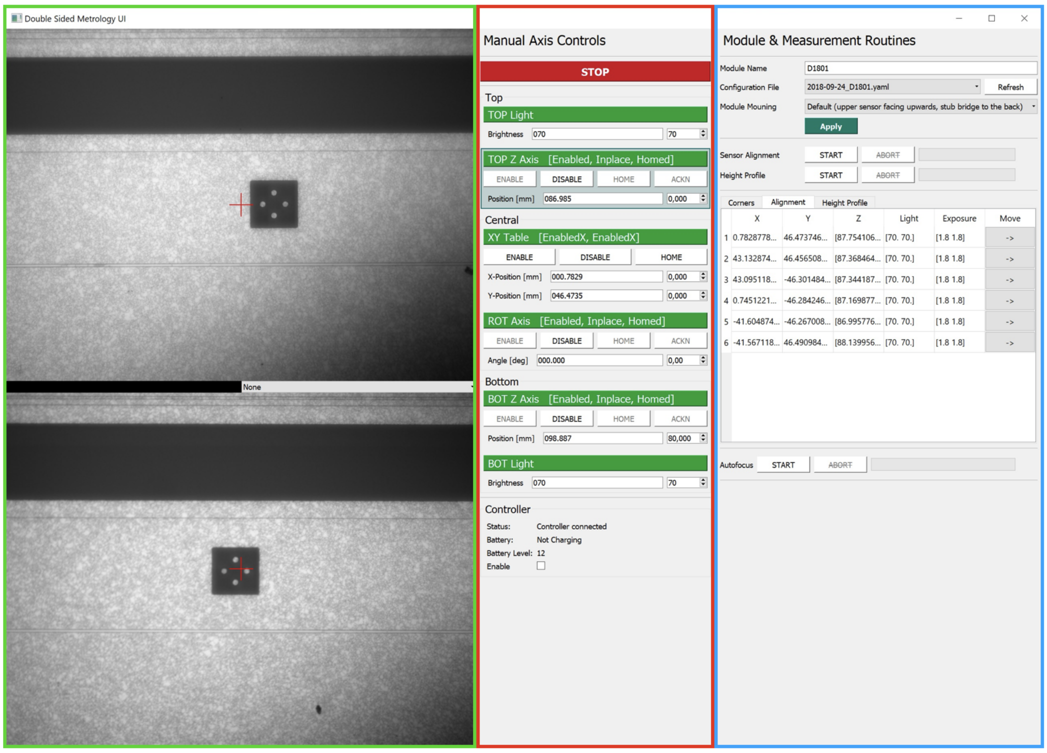

Figure 3.11: A screenshot of the GUI in the state at the beginning of this work. In live images of both cameras are shown in the green frame, the manual axis controls in red, and the module and measurement routines in blue.

All movements of the machine, even during measurement, can immediately be interrupted with the large red "STOP" button on the top of the panel. The button should be used in case of emergency. After a restart of the machine or after pressing the emergency button, the stages have to move to their "home position" separately. For that, the camera axes and both axes of the xy-table move to its maximal range of traveling and find the home position. The rotation table has to be within $\pm 20°$ around the $0°$ position to push the "HOME" button. The stage then automatically moves to the zero position. If the stage is outside the $\pm 20°$ interval and the "HOME" button is clicked, the rotation stage will move into its upper or lower limit, causing an error. If that happens, the "ACKN" button has to be pushed. The button disables the axis. The rotation axis then can be turned out of an error position by hand and be enabled again.
Enabled stages can also be operated with a Sony Dualshock 4 controller [24]. With its arrow keys, one can select the stage desired to move. The joystick can be used to move the selected axis. This is more comfortable than moving the stages by entering values, especially when the user wants to look for something on the module. A check mark next to "Enable" on the bottom of the panel indicates that the controller is connected and ready for operation.

The module and measurement routines

Before starting a measurement, it has to be configured. The user has the option to enter a module name. A configuration file has to be selected. This special file contains information about the locations of the four pins on which the module is mounted. The mounting positions are used to define a multi-step transformation from the sensor model to the xy-stage. The transformation also accounts for a possible 180° rotation of each sensor. A rotation of a sensor needs to be defined in the configuration file. The file also contains information about the height at which each pin is in focus in the upper and lower cameras. With these heights, one can predict the height at which the sensor should be seen sharply. The camera settings also have to be entered into the configuration file. The "Refresh" button updates the configuration file list and must be used if changes were made to the file while the GUI was open. The orientation of the module is given in the "Module Mounting" field. The position in which the upper sensor faces upwards and the so-called stump bridge carrying the SEH points to the back of the DSM was chosen as the "Default" orientation.

Pressing the "Apply" button executes the transformation from the sensor model to the xy-stages and lists various positions in the window below. Under the "Alignment" tab, for example, the x and y positions in the xy-stage, the height of both cameras and their settings are displayed corresponding to the positions selected for the alignment measurement (Section 3.4.1). By clicking on the arrow to the right of each position, the stages move to the corresponding place. This way, the user can check if the selected positions are reasonable. If everything is set up, a push on one of the "START" buttons starts the respective measurement routine. With the "ABORT" button, the measurement can be stopped. A progress bar next to it indicates the progress of the measurement.

Below the position window, the "Autofocus" of the DSM can be started. For that, the cameras move within a predefined interval around the current position of the respective camera axis. During the movement, images are continuously captured. By comparing the gray level differences between the pixels, the sharpness at each height can be quantified. A sharper image has more detail and therefore higher gray level differences. If the height of the sharpest image is in the upper or lower fifth of the interval traversed, the autofocus is repeated with the interval extended in that direction. This is to ensure that there is no sharper position directly above the interval initially traversed. If the sharpest position is in the middle 3/5 of the interval, the cameras move to the determined position and reliably show a sharp image.

The autofocus can be used with any z position. In fact, both original DSM measurements (Section 3.4) rely on the autofocus functionality at different steps. In this case, the autofocus is used after the camera axis moved to a desired height, which is roughly the height at which a specific object is in focus.

3.4 The DSM Measurements

This chapter explains the measurement routines and their analysis developed by Marius Preuten and Christian Käseberg. The presented routines run fully automatically and only need to be configured correctly.

3.4.1 The Alignment Measurement

With the alignment measurement, it is checked if the relative orientation of the two sensors of a 2S module fulfills the precision requirements presented in Section 2.3.1.

The routine

Before the measurement, the user defines in the configuration file how many and which points should be considered. For this purpose, a sensor mask is used, which includes the positions of various features on the sensor that will later be detected in the images. At least some features must be visible at the selected positions; this can be a simple alignment marker but also something more complex.
The desired positions are then transformed from the sensor mask coordinates to xy-stage coordinates. With the start of the measurement routine, the rotation table moves to its null position, the xy-stage moves to the first defined position, and the cameras move to a height calculated from the configuration file that is relatively close to the height at which the sensors can be seen in focus. Afterwards, the autofocus searches for a sharp image in both cameras. In the next step, the rotation stage moves to its upper limit of $+200°$. While rotating the other way around to the $-180°$ position, the camera constantly takes pictures. A total of 72 images of the upper and lower sensor are captured per side, which are then stored. The rotation stage moves back to its null position before the xy-stage moves to the next position and the described process is repeated. This is done until pictures are made at all defined positions. Figure 3.12 shows a collection of images made at one point of the upper sensor during the measurement, illustrating the rotation. Information about the measurement is combined in a so-called "asdf" file used for the analysis.

The analysis

The alignment analysis method finds the positions of the rotation axis on the lower and upper sensors. For this, the sensor mask is fitted to 16 out of the 72 pictures captured during the rotation of each sensor at each position. The images are selected based on a circle divided into 16 points with equal angular distances. For each point, the angles at which the 72 images were taken are sorted by increasing distance from the angle of the point. The image with the smallest angular distance to the point is preferred. If the method of mask matching to the image fails, the image with the next smallest distance to the respective point is used. In this way, the 16 points that are fitted are distributed relatively evenly on a circle in most cases. The sensor mask is restricted to a $1.6 \times 1.6\,\mathrm{mm}^2$ square around the intended point of rotation, defining the portion of the sensor mask that should be fitted. The side length is roughly the same as the width of the pictures with 1600 pixels, which is about 1.3 mm. The position to be restricted in the sensor mask is predefined in the configuration file and respects the orientation of the module in the setup.
To prepare the selected pictures for the fitting of the sensor mask, a Canny edge detection

[25] is performed to identify the edges of features visible in the images. This is followed by a so-called Hough transform [26] that finds the positions where the edges cross.
In the next step, the defined portion of the sensor mask is fitted to the processed pictures. The sensor model is given in units of mm, the picture in pixels. The model is thus scaled accordingly. The fitting process determines how much the sensor mask has to be rotated and shifted in order to match each individual picture. Figure 3.13 shows an example of one raw image and the mask fitted to the processed picture.
If all transformations are successful, the 16 positions form a circle with the rotation axis in the middle. Therefore, a circle fit is performed to those 16 positions, resulting in the coordinates of the rotation axis (Figure 3.14).

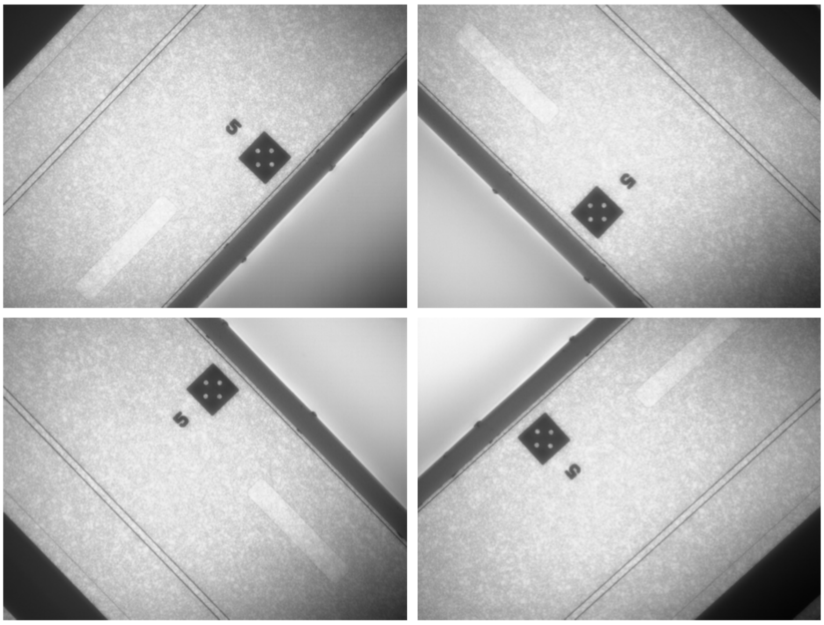

Figure 3.12: Four of the 72 images captured on one point the lower sensor during the measurement.

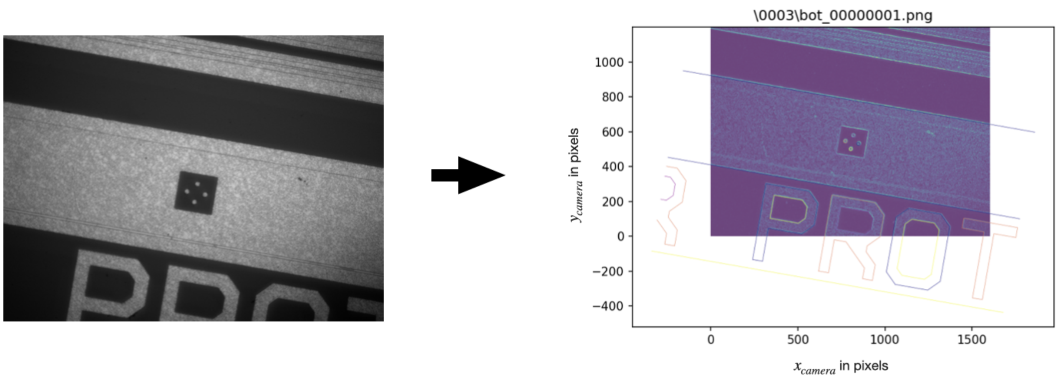

Figure 3.13: On the left is a raw image taken during the rotation. On the right is the version of the same image after the Canny edge and Hough transforms. Also, the features of the sensor mask fitted to the image can be seen.

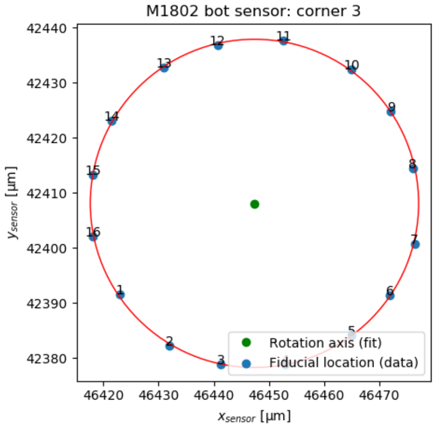

Figure 3.14: An example of a circle fit to the 16 positions found from the sensor mask fitting.

This is done for each sensor and each measurement point. Finally, the resulting coordinates of the rotation axes on the upper sensor and the lower sensor are used to fit the upper sensor onto the lower one to define their orientation with respect to each other (Figure 3.15).

The coordinate system in which the results from the alignment analysis are given has its origin in the middle of the lower sensor (Figure 3.16). It is oriented such that the x-axis points away from the SEH, and the y-axis is rotated 90° counter-clockwise to the x-axis. The z-axis is oriented such that a right-handed coordinate system is formed. Then, the difference in x gives the offset perpendicular to the strips, and the y-difference represents the offset along the strips. The positive direction of rotation is also counter-clockwise. Example results for a DSM

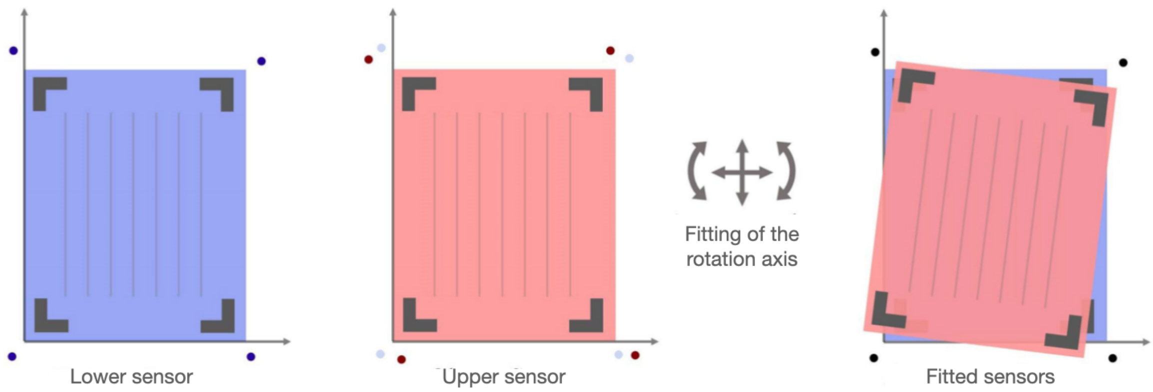

Figure 3.15: A scheme for the matching of the rotation axes of the upper sensor to the lower sensor. In the second image, the rotation axes of the lower sensor are shaded blue and indicate where the upper sensor must move. Modified from Ref. [27].

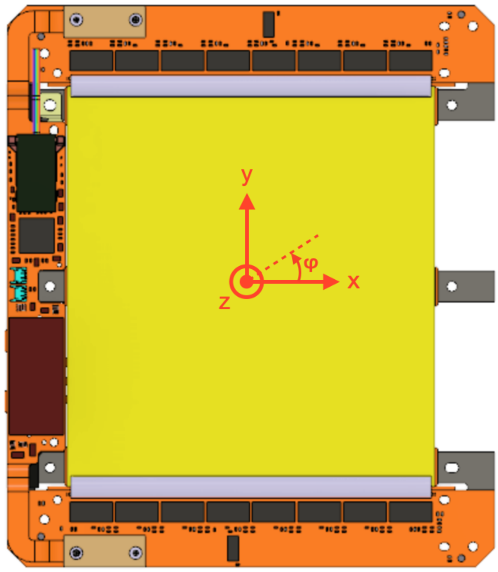

Figure 3.16: A schematic representation of the coordinate system in which the DSM alignment results are given. The z-axis points out of the screen.

measurement of a 1.8 mm module (M1802[1]) are:

$$\Delta x = (-4.9 \pm 0.1\, stat. \pm 2.2\, syst.)\ \mu\text{m}$$
$$\Delta y = (-8.0 \pm 0.2\, stat. \pm 2.2\, syst.)\ \mu\text{m}$$
$$\phi = (+29 \pm 3\, stat. \pm 4\, syst.)\ \mu\text{rad}.$$

Origins of the uncertainties are discussed in Section 4. The measured orientation of the sensors of this module is clearly within the specifications, which is representative for all modules built so far in Aachen.

3.4.2 The Height Profile Measurement

Due to the small depth of focus of the cameras, the DSM can be used to measure a height profile of a module because height differences of the camera reflect height differences in the module.

The routine

To be able to relate the camera positions to each other later in a meaningful way, the z-positions of the upper and lower cameras must be calibrated. This is done by focusing on the same object with both cameras. The DSM setup uses a glass plate that is glued to the carbon fibre plate. Dust or other contaminants on the glass can be detected by both cameras.
In the next step, the lower surface of each of the four mounting pins is focused one by one.

[1]The second built prototype of a 1.8 mm module.

In the configuration file, the user specifies at how many positions the height should be measured. Usually 6 x 7 measurement points are taken in x x y direction. The measurement starts at the bottom left side of the module. Both cameras are autofocused before moving to the next point. The xy-stage moves through a grid distributed over the module surface, constructed with equal distances in x and y between each point. The user can define an offset from the sensor edges if parts of the module are not to be viewed. This is useful if the module is encapsulated, for example.
In each calibration and measurement step, the z positions of the cameras and the xy-stage positions are stored. One measurement with 42 points takes about half an hour.

The analysis

From the measurements on the glass plate, the z-position of the upper camera is related to the z-position of the lower camera. The mounting surface of the module serves as a reference plane and is calculated from the pin heights. The height of the mounting surface is calculated from the z-positions of the lower pin surfaces and the individual height of each pin. The resulting heights of the mounting points are then used to fit a plane to them. Height differences are then calculated with respect to this plane but also between the upper and lower sensor. Example result plots are shown for a 1.8 mm module with a 6 x 7 points measurement (Figure3.17a) and for a 4 mm module with a very detailed 12 x 12 points measurement (Figure3.17b). By design, the values represent the height difference between the top of the upper sensor and the bottom of the lower sensor. The modules are slightly thicker in the center than on the left and right, where the sensors are glued to the spacers. The measurements can confirm an expected height difference from the gap size between the two module types.

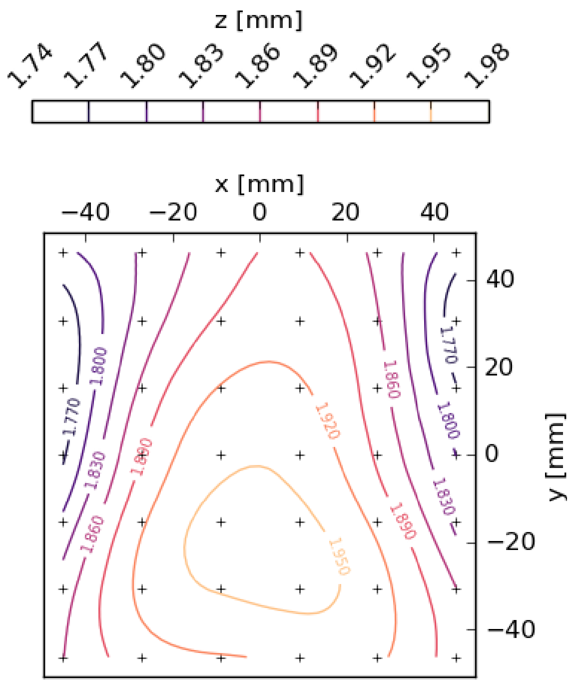

(a) 1.8 mm gap size module

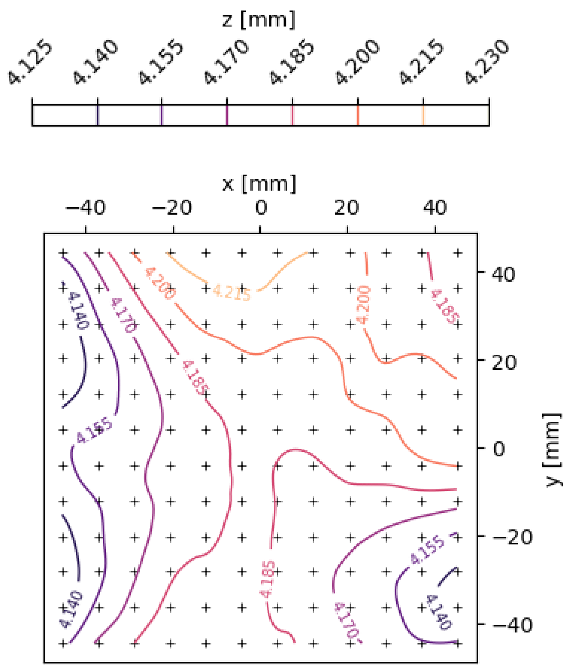

(b) 4 mm gap size module

Figure 3.17: Measured height profiles of a 1.8 mm module with 42 measurement points (a), and of a 4 mm module with 144 points (b). The lines indicate areas of equal height and are calculated from the measurement points.

4 Alignment Measurement Uncertainties

This section presents the statistical and systematic uncertainties related to the alignment measurement result. Therefore, the statistical uncertainty from several measurements is calculated first. Then, different influences on the systematical uncertainties are discussed.

4.1 Statistical Uncertainty

To quantify the statistical uncertainty, it is necessary to check how much the values vary when alignment measurements are performed on the same module. Between each measurement, the module is removed from the pins and remounted. Fourteen measurements were taken on different days with module M1802, nine on the first (Table 4.2) and five on the second (Table 4.3).

The variance is calculated for both series of measurements. Since the measurements fluctuate around different mean values but represent the same statistic, they can be combined with a weighted average:

$$\sigma_{\mathrm{tot}}^2 = \frac{(n_1 - 1) \cdot \sigma_1^2 + (n_2 - 1) \cdot \sigma_2^2}{(n_1 - 1) + (n_2 - 1)}.$$

This results in the following values for statistical uncertainties, rounded to the first significant digit:

$$\sigma_{\Delta x,\mathrm{stat}} = 0.1\,\mu\mathrm{m}, \qquad \sigma_{\Delta y,\mathrm{stat}} = 0.2\,\mu\mathrm{m} \quad \text{and} \quad \sigma_{\phi,\mathrm{stat}} = 3\,\mu\mathrm{rad}.$$

In addition, the statistical uncertainty for measurements without remounting the module between measurements is estimated using five measurements with module M1802. The results are summarized in the Table 4.4 and show a lower statistical uncertainty for all variables than the measurements in which the module is remounted between each measurement.

Measurement	ϕ [µrad]	Δx [µm]	Δy [µm]
1	29.2	−4.73	−7.94
2	32.7	−4.93	−8.04
3	27.5	−4.61	−8.39
4	33.6	−4.76	−7.95
5	28.8	−4.76	−7.99
6	28.5	−4.67	−8.23
7	28.0	−4.68	−8.20
8	30.0	−4.78	−7.96
9	31.5	−4.73	−8.11
Standard deviation	2.2	0.09	0.16

Table 4.2: Nine measurements with module M1802 and four measurement points, remounting it after each measurement. In the last row, the standard deviation is shown. The angle ϕ represents the counter-clockwise rotation of the upper sensor with respect to the lower sensor, Δx is the translational shift perpendicular to the stripes, and Δy is the translational displacement parallel to the stripes.

Measurement	ϕ [µrad]	Δx [µm]	Δy [µm]
1	27.9	−5.06	−7.62
2	29.8	−5.16	−7.73
3	26.1	−4.87	−7.53
4	34.9	−5.14	−7.34
5	26.8	−5.15	−7.95
Standard deviation	3.6	0.12	0.23

Table 4.3: Five measurements with module M1802 and four measurement points, remounting it after each measurement. In the last row, the standard deviation is shown.

Measurement	ϕ [µrad]	Δx [µm]	Δy [µm]
1	24.6	−4.99	−8.08
2	24.6	−4.94	−7.96
3	26.3	−4.87	−7.98
4	28.0	−4.92	−8.03
5	25.5	−4.97	−8.07
Standard deviation	1.5	0.05	0.05

Table 4.4: Five alignment measurement results of the module M1802, performed with the exact same settings and without remounting it between the measurements. In the last row, the standard deviation is shown.

4.2 Systematical Uncertainty

The idea of systematic uncertainty analysis is to measure the module in one configuration and then change it slightly to study the effects on the results. In this procedure, the module is not touched. Therefore, the statistical uncertainties:

$$\sigma'_{\phi,\text{stat}} = 1.5\,\mu\text{rad}, \qquad \sigma'_{\Delta x,\text{stat}} = 0.05\,\mu\text{m} \quad \text{and} \quad \sigma'_{\Delta y,\text{stat}} = 0.05\,\mu\text{m},$$

conducted from Table 4.4 are used when assessing the significance of any systematical effect. The variance, especially for the translation, is so small that even tiny effects should be noticeable.
Three different influences are investigated that could affect the measurement systematically:

- A tilt of the camera with respect to the sensor surface.
- A tilt of the module mount with respect to the camera.
- The scale factor from pixels to µm.

An angle between the sensor surface and the camera would cause the captured images to be compressed (a module standing perpendicular to the xy-stage and parallel to the y-axis would have no width in the picture). Additionally, if there is a tilt, for example around the y-axis of the stage, distances traveled on the sensor along the x-direction are larger than distances along the y-axis due to the angle.
In contrast, the influences of an image that is not properly centered, e.g. due to an incorrect mounting position, should not affect the results since such a shift is canceled out when rotating the module during the measurement. This was verified in two different ways: by physically moving the carbon fiber mounting plate without adjusting the configuration, and by intentionally setting an incorrect position of a pin in the software. Both have the effect of an image being displayed that is shifted from the initial image. The measurement results show no statistical significance, so these sources can be excluded as a source of systematic errors.
The magnitudes of the proposed influences are discussed separately in the following using measurements on module M1802.

Camera tilt

The cameras of the DSM setup are equipped with a screw with which they can be moved a small amount to adjust the field of view (Figure 4.18). Adjusting the image also changes the angle between the sensor and the camera. This influence is analyzed by examining the effects on the results of a measurement where the camera is shifted relative to a measurement where the camera axis is approximately aligned with the axis of rotation. The magnitude of the shift is chosen so that the features of interest are just visible to the cameras at each point. Figure 4.19 shows an example of the magnitude of the left-right shift in both directions by superimposing the original image and the shifted image. Table 4.5 shows the measurements

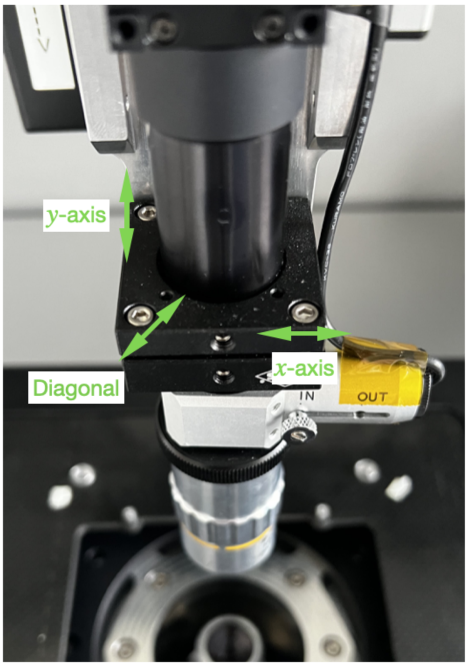

Figure 4.18: A photograph of the upper camera. The arrows indicate which screw shifts the camera in which direction.

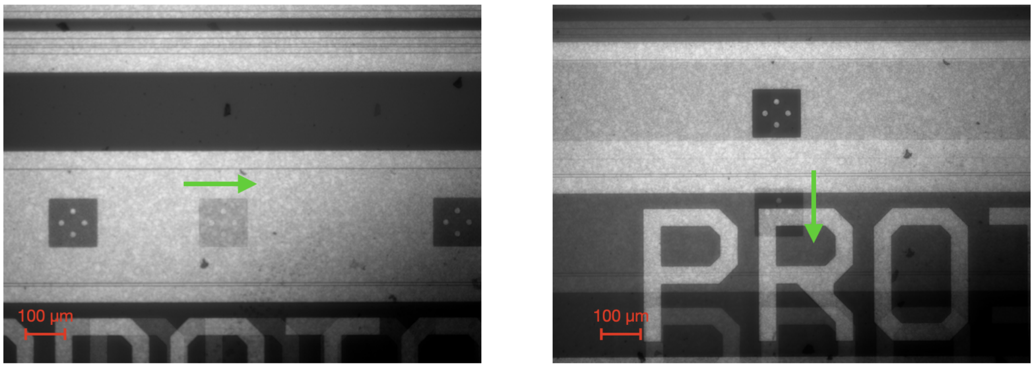

Figure 4.19: Size of the camera shift relative to the shaded position. In the left picture, the camera is moved to the right (indicated by the green arrow) such that the image shifts to the left by about 330 µm. The right picture shows the situation for the camera moved down by roughly 240 µm.

for the camera tilt effect. Note that for the up-down shift, only the downward part could be analyzed since no significant upward change was possible that would still have yielded a meaningful measurement. Also, the x- and the y-axis of the xy-table are swapped with the respective axes in the result coordinate system. Therefore, shifting the camera to the right should influence the Δy result in the measurement and vise-versa.

The results do not show any significant effect on the rotation with respect to their reference measurement. But the rotation varies a lot between the reference measurements, which were taken on different days. The reason for a systematical change of the ϕ results over time could not be found during this work, but the effect was also observed for other modules. However, the systematical uncertainty of this effect is estimated from both reference measurements as half the difference of the two values of the rotational shift:

$$\sigma_{\phi,sys} = \frac{(31.8\,\mu\text{rad}) - (24.6\,\mu\text{rad})}{2} \approx 4\,\mu\text{rad}.$$

Each camera shift has an effect on the two results Δx and Δy that is larger than the statistical fluctuation. Since the widths of the images are bigger than their heights, the camera could not be shifted as far down as it could be shifted to the left and right.

The systematic error contribution to Δy is estimated to be half the difference between the results of the camera shifted to the left and right:

$$\sigma_{\Delta y,\text{cam}} = \left| \frac{(-7.80\,\mu\text{m}) - (-7.32\,\mu\text{m})}{2} \right| \approx 0.24\,\mu\text{m}.$$

The contribution to Δx is computed from the downshift of the camera. Since meaningful measurements for the up-down shift of the camera could only be provided for the downshift, Table 4.5 reveals only half effect on Δx. As stated earlier, the camera offset for the up-down shift had to be chosen smaller to provide meaningful results. Assuming that the effect on the results scales linearly with offset, the measured effect should be a fraction of $\sigma_{\Delta y,\text{cam}}$ corresponding to the size of the shifts:

$$\sigma_{\Delta x,\text{cam,scaled}} = \sigma_{\Delta y,\text{cam}} \cdot \frac{240\,\mu\text{m}}{330\,\mu\text{m}} = 0.175\,\mu\text{m}.$$

	ϕ [µrad]	Δx [µm]	Δy [µm]
Reference for left-right shift	31.8	−4.37	−7.66
Camera shift to the right	29.9	−4.13	−7.32
Camera shift to the left	32.3	−4.46	−7.80
Reference for up-down shift	24.6	−4.27	−8.51
Camera shift down	24.1	−4.10	−8.36

Table 4.5: The results of the effect of a camera shift on the results. The measured values correspond to the scenario described in the first column.

	ϕ [µrad]	Δx [µm]	Δy [µm]
No height change	31.8	−4.37	−7.66
Upper left	34.4	−2.53	−6.58
Lower left	31.5	−6.77	−6.44
Both left	34.6	−4.89	−5.55
No height change	27.0	−5.32	−7.84
Right screw	26.0	−5.29	−10.07

Table 4.6: Measurements of the influence of an inclined mounting surface on the results. The first column indicates which screw was rotated. A new reference measurement was taken for the measurement with the right screw.

This is almost exactly what is obtained as an estimate from the Δx values of the respective camera shift from table 4.5:

$$\sigma_{\Delta x,\text{cam}} = |(-4.27\,\mu\text{m}) - (-4.10\,\mu\text{m})| = 0.17\,\mu\text{m}.$$

Therefore, the systematical uncertainty on Δx is estimated to be the same as $\sigma_{\Delta y,\text{cam}}$. So the final contribution of a tilted camera with respect to the sensor surface is:

$$\sigma_{\Delta x,\text{cam}} = 0.24\,\mu\text{m} \qquad \text{and} \qquad \sigma_{\Delta y,\text{cam}} = 0.24\,\mu\text{m}.$$

Module mount tilt

The height of the carbon fiber plate with the mounting pins can be adjusted with screws (Figure 4.20). The upper left screw rotates the plate around an axis that points from the lower left edge of the carbon fibre plate to the upper right edge. Respectively, the lower left screw turns the plate around the diagonal pointing from the upper left edge to the lower right edge. The plate is rotated around the y-axis by using both left screws or the right screw. The plate is tilted about each axis until a tilt is visible to the user by eye, which is the case after half a screw turn. These measurements are compared with results without height change (Table 4.6). A turn around the y-axis of the stage is expected to influence the Δy result, because

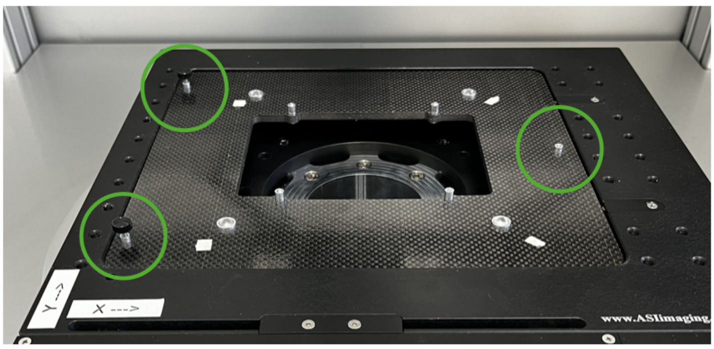

Figure 4.20: The height screws on the xy-table are highlighted with green circles.

distances are distorted in the x-direction of the xy-stage when rotating around the y-axis. A turn of the upper left screw or the lower left screw is expected to influence both translational shifts. However, due to construction, the sign of the effect on Δy should be the same for both scenarios. In contrast, the impact on Δx is expected to have opposite signs.
This behavior can be confirmed by the results. A systematical effect on the rotation is smaller than the statistical uncertainty when looking at the results with respect to their reference measurement.
The systematical uncertainty contribution to the Δx results is estimated to be half the difference of the Δx values that result from the upper left and lower left screw turn:

$$\sigma_{\Delta x,\mathrm{mount}} = \left| \frac{(-6.77\,\mu\mathrm{m}) - (-2.53\,\mu\mathrm{m})}{2} \right| \approx 2.12\,\mu\mathrm{m}.$$

The contribution to the Δy results is estimated as the difference of the Δy values of the measurements of both left screws and the right screw to their respective reference measurement:

$$\sigma_{\Delta y,\mathrm{mount}} = \left| \frac{((-10.07\,\mu\mathrm{m}) - (-7.84\,\mu\mathrm{m})) + ((-7.66\,\mu\mathrm{m}) - (-5.55\,\mu\mathrm{m}))}{2} \right| \approx 2.17\,\mu\mathrm{m}.$$

Since the results are about the same, the mean of both values is used as an estimate of the influence of a tilted module mount on the systematical uncertainty of both translational shifts:

$$\sigma_{\Delta x,\mathrm{mount}} = 2.15\,\mu\mathrm{m} \qquad \text{and} \qquad \sigma_{\Delta y,\mathrm{mount}} = 2.15\,\mu\mathrm{m}.$$

Scale factor

The scaling factor is set individually for each analyzed image (16 of each side per measurement point). Since the module is not mounted perfectly flat, the height at each measuring point is slightly different. Therefore, the scaling factor is also different at each point. For example, in the case of the M1802 module, the factor varies between 1.279 Pixel/µm and 1.289 Pixel/µm at different points on the module. The scale factor of the 16 images taken at the same point during rotation differs on the order of 0.0001 Pixel/µm. The error contribution is estimated by varying the scale factors at different positions in all possible constellations. For example, at measurement position 2, the highest of the 16 scale factors was selected for both the upper and lower sensors. Then the measurement was reanalyzed using the highest scaling factors for all 16 images of the upper and lower sensor, while the default scaling factors were used for every other image. The results are shown in Table 4.7, representing all other combinations. Any effect on the results is smaller than the statistical fluctuation.
The combination of all systematical influences on the Δx error is:

$$\sigma_{\Delta x,\mathrm{sys}} = \sqrt{\sigma^2_{\Delta x,\mathrm{cam}} + \sigma^2_{\Delta x,\mathrm{mount}}} \approx 2.2\,\mu\mathrm{m}.$$

The error on Δy is the same. Together with the estimation of the systematical uncertainty of the rotation, this leads to the final result for the total systematical uncertainty of the alignment

	ϕ [µrad]	Δx [µm]	Δy [µm]
No change of scale	26.3	-4.87	-7.98
Highest scale at Position 2	25.8	-4.83	-7.99

Table 4.7: Measurement showing no effect when varying the scale factor.

measurement of:

$$\sigma_{\Delta x,\mathrm{sys}} = 2.2\,\mu\mathrm{m}, \quad \sigma_{\Delta y,\mathrm{sys}} = 2.2\,\mu\mathrm{m} \quad \text{and} \quad \sigma_{\phi,\mathrm{sys}} = 4\,\mu\mathrm{rad}.$$

5 Improvements of the DSM Setup

This section first presents the improvements to the user interface that enhance the usability of the program, followed by the improvements to the alignment measurement routine that were introduced as part of this work.

5.1 Extensions to the GUI

Target folder to store measurement

The name of a module under which the results should be stored had to be entered in the configuration file. To make the DSM setup as user-friendly as possible, it is desired that everything can be controlled via the GUI. For this purpose, it was added that the measurement is saved under the name entered in the text field next to "Module name" in the upper right corner of the GUI. If no name is entered, the measurement is saved in the folder specified in the configuration file.

Running the analysis from the GUI

Before this work, one had to switch from the GUI to the console and manually enter the analysis method and the location of the corresponding asdf file. The results would then show up in the console as raw values without units or a variable name.
To make the start of the analysis more accessible, a button has been added that allows the user to start the analysis from the GUI. Clicking the button opens the DSM results folder. It allows the user to select an asdf file of an alignment or height profile measurement and starts the corresponding analysis with the selected file. Next, the results are displayed with units and a variable name on the user interface. In addition, the results are highlighted in green if they meet the accuracy requirements and in red if they do not. Finally, the results are stored in a text file so that they can be reviewed at any time.

Measured values sketch

For the user to know which measurement value corresponds to which physical distance, sketches have been drawn, which are displayed when the GUI is opened (Figure 5.21). Details about the measurements can be found in Section 3.

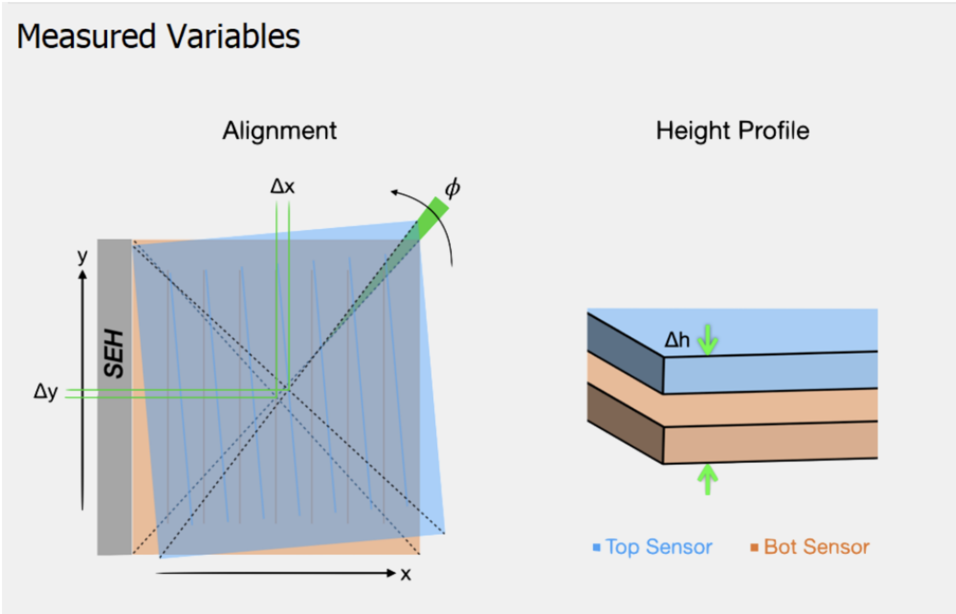

Figure 5.21: A sketch added to the user interface that graphically illustrates the exact definitions of the measured parameters.

5.2 Performance Improvements

The goal is to perform alignment measurements on four modules a day during the production phase. To save time, the measurement should be as fast as it can get without losing measurement precision.

The autofocus that has to be performed at each measurement point is one of the driving factors for the measurement time. If the setup is well configured, the predefined height to which the cameras should move at each point already corresponds to a height at which the desired image is relatively sharp. Then the autofocus only needs to make one iteration at each point to find a clear image, reducing the measurement time. The predefined heights of the camera axes are configured using the mounting pins because their height is close to the height of the sensors. The upper camera is configured by finding the sharpest point of each mounting surface of each pin in the camera. The height of the sensor is then the sum of the configured height, the spacer thickness, and the sensor thickness. The lower camera is configured using the bottom surface of each pin. The height of the sensor in the bottom camera is the height of the pin added to the configured height minus the sensor thickness. Table 5.8 summarizes the chosen heights of each pin.

Prior to this work, the autofocus was coded to first search for a sharp image at each point in a coarse interval, followed by a fine search. It turned out that the coarse search already reliably found a sharp image, so the fine search was excluded from the measurement.

Due to the reduction of two autofocus routines to one and the autofocus of both cameras needing only one iteration at each measurement point due to the improved settings, the time it takes the autofocus to find a sharp image could be reduced from about 60 seconds to about 10 seconds. This reduced the total measurement time from 10 minutes and 30 seconds to about

	Upper left	Upper right	Lower left	Lower right
Upper camera height [mm]	85.134	85.139	85.144	85.159
Lower camera height [mm]	88.788	88.697	88.781	88.748

Table 5.8: Configured z-positions of the cameras at each mounting pin. The height of the upper camera corresponds to the position at which the mounting surface of the pin is in focus. The respective height of the lower camera is the point at which the bottom surface of the pin is in focus.

7 minutes. Additionally, a bug could be fixed that sometimes caused one or both cameras to freeze during the alignment measurement, which led to a crash of the routine. It was found that this can occur after each rotation at every measurement point due to the frame rate being updated from 10 fps to 40.66 fps. The frame rate was lowered for the rotation to keep the memory usage at an acceptable level during image taking. The change of the frame rate has been excluded so that it always is at 10 fps. This resolves the bug and still delivers a smooth live image in the GUI.

6 Cooling Tests with the DSM Setup

A major interest regarding the new 2S modules is the behavior of their sensor-to-sensor alignment at low temperatures, since the modules in the experiment are cooled with −35°C cold CO_2. With the standard DSM machine, the orientation could only be measured at room temperature. As part of this work, the DSM setup was extended to allow measurements down to temperatures of −10°C.

6.1 Setup Enhancements

For the alignment measurement to be fully functional, the cameras must focus on the sensor, and the stages must be able to move freely. The challenge was to maintain this functionality while cooling down the module. The individual parts that allow measurements at low temperatures are presented in the following.

The box with glass plates

The module is cooled down with air. To keep the module in contact with the cold air long enough, a box was designed with CAD and 3D printed out of plastic (Figure 6.22). The box is designed so that glass plates fit on the top and in a cutout at the bottom. Glass is used so that the cameras can still capture images of the module. The DSM setup limits the size of the box. It measures 215 x 225 mm^2 in width and length so that it fits on the carbon fibre insert of the xy-table. A height of 35 mm was chosen so that the upper camera could still move close enough to the module.

The upper glass plate is 4 mm thick and the lower one is 3 mm thick. The upper glass plate must be thin enough to allow the upper camera to move close enough to the module. The lower plate has four manufactured holes, which are aligned with the four mounting pins of the carbon fibre insert when the glass plate is placed in the cutoff of the box. The glass on the bottom should be as thin as possible because the pins still have to reach over the bottom glass surface, to be able to mount the module. The manufacturer was able to provide a 3 mm thick glass plate with holes, which is sufficient.

For the cold air to get out of the box again, small cutoffs are placed at various positions. All of the inner plastic parts of the box and the outer wall are insulated with sticking ArmaFlex [28].

The cooling system

Figure 6.23 illustrates the cooling system schematically. A cooling machine cools down liquid ethanol to temperatures of about −24°C. The cold ethanol flows through insulated tubes into a heat exchanger and back into the cooling machine. Dry air from the laboratory flows through the other part of the heat exchanger. The cold, dry air continues through insulated tubes into the box, cooling the module. The cold air is released uniformly from tubes with holes to avoid temperature gradients in the box. The tubes are placed at the edges of the box so that the air flows in from all directions (Figure 6.24). The tube connecting the box to the heat exchanger

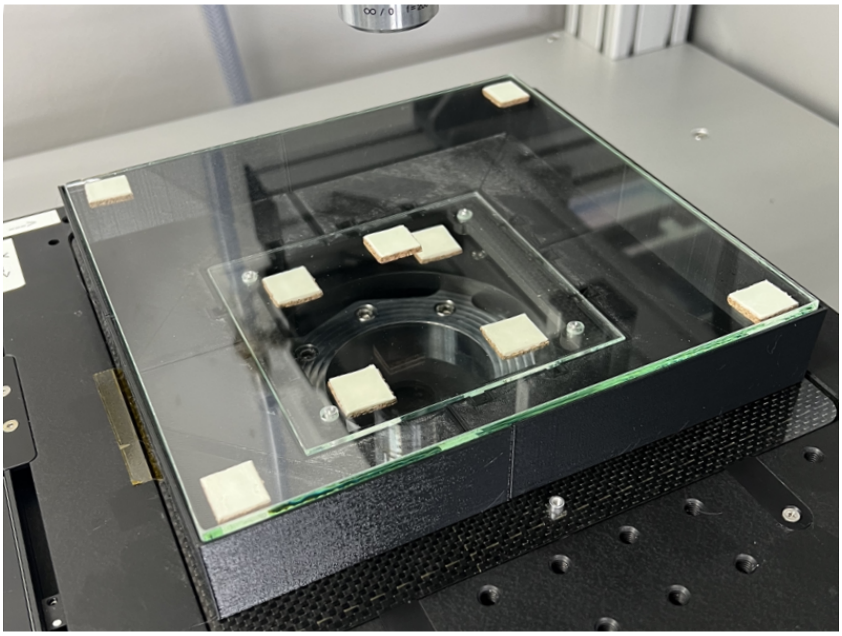

Figure 6.22: A photograph of the 3D printed plastic box with glass plates at on the upper and lower side. The box fits on the xy-table.

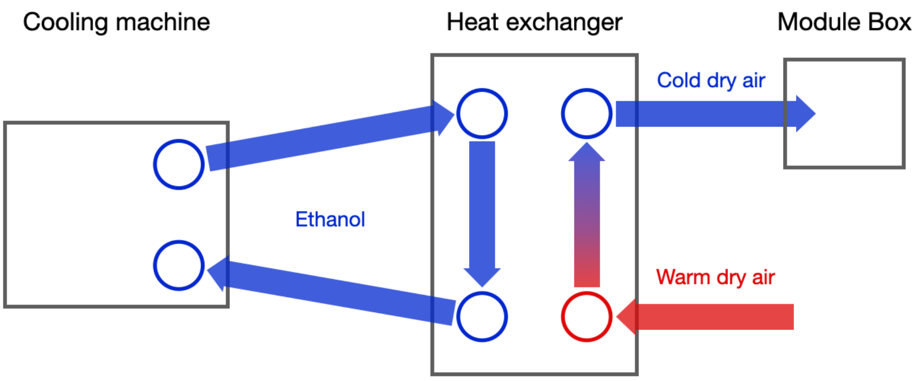

Figure 6.23: A sketch of the cooling source for the DSM setup. A heat exchanger is cooled down by a cooling machine. Dry air flows through the heat exchanger and is also cooled down. The module is flushed with cold dry air.

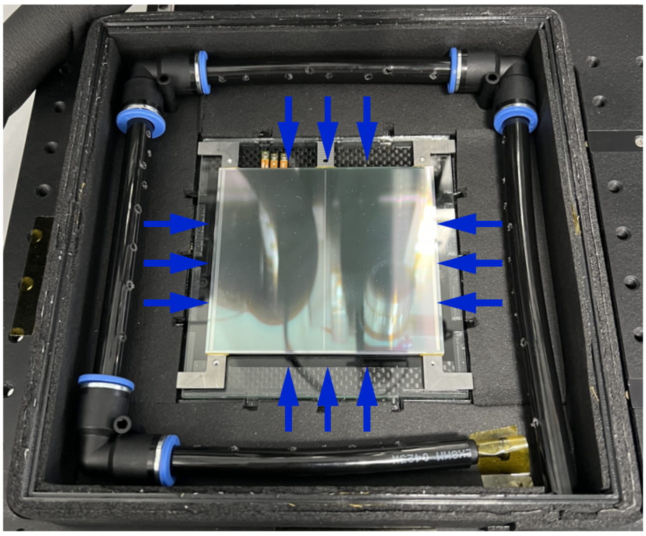

Figure 6.24: A photograph of the box with the tubes distributing the cold dry air inside evenly.

lies in the aluminum frame of the DSM and is trailed by the rotation stage. The tube must be long enough and elastic to minimize interference from a clean rotation, so a silicone tube is used.

All cold air-carrying tubes and the heat exchanger are insulated with ArmaFlex.

The covering

The relative humidity relates the current amount of water vapor in a given area of air to the maximum amount of water vapor that this area can hold at a given temperature. Once this value exceeds 100 %, the so-called dew point is reached, causing the excess water to condense when the temperature is lowered further.

This behavior must be considered in the DSM setup for cold tests and is why dry air is used in the first place. When the temperature in the box drops below a specific temperature, the glass plates become so cold that the surrounding lab air condenses on the top glass plate, preventing the upper camera from being able to capture the sensor surface. This problem does not occur with the lower glass plate because some of the dry air flows down through the bottom of the box, where space is limited such that the dry air flow creates a sufficiently dry environment to prevent condensation. The entire top of the DSM is covered by a custom-made cardboard box, creating a relatively small volume around the box but still allowing all stages to move freely (Figure 6.25). The dry air exiting the top of the cold box flushes this volume, shrinking the amount of water and thus the relative humidity and preventing water condensation on the top glass plate.

The monitoring

To monitor the temperatures in the box, the cardboard box and the heat exchanger, four PT1000 temperature sensors are used. One is located under the insulation of the heat ex-

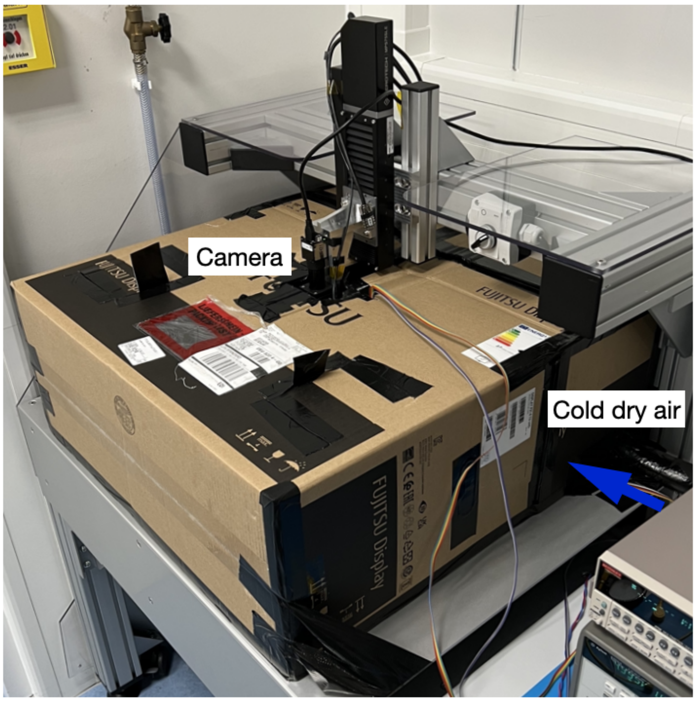

Figure 6.25: A photograph of the customized cardboard covering the cold box. The carton is big enough for all stages to move freely. A cutoff in the top leaves space for the upper camera and its axis. The tube with the cold, dry air is inserted through a hole visible in the lower right of the picture.

changer near the port from which the dry air exits. Another temperature sensor is located in the cardboard volume. The last two sensors are located inside the cold box. During the cold test of module M1802, one sensor was attached with thermal paste to the stump bridge of the module (Figure 6.26) to track the module's temperature as accurately as possible. The other one was placed near the left edge of the box. The measurement showed that the module temperature was the same as the temperature in the box. In all other cold tests performed, the first sensor was placed in the box near the stump bridge rather than on the stump bridge, as it was easier to install.

Two Honeywell HIH-4000 series humidity sensors [29] are used to measure the relative humidity inside the cold box and the cardboard volume. The humidity sensors are placed in the direct vicinity of a temperature sensor to obtain a meaningful value since the relative humidity depends on temperature. The humidity sensor is placed next to the second temperature sensor in the cold box.

The temperature sensors measure resistances, and the humidity sensors measure voltages that have to be converted into temperatures and relative humidities. The electrical signals are measured with a digital multimeter [30]. For this purpose, a LabVIEW program was used, which also displays and stores the measured values of all sensors.

During final assembly, the module is fixed to the mounting pins with screws tightened to

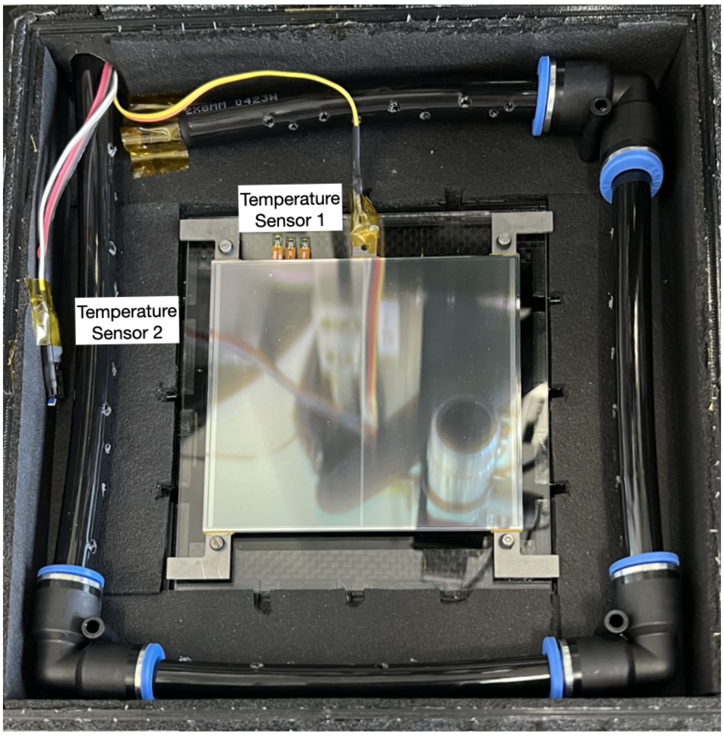

Figure 6.26: A photo, showing the locations of both temperature sensors during the first cold test with module M1802.

a torque of 1 cNm using a torque screwdriver. The mounting pins are in contact with the carbon fiber plate, which is not cooled. The pins therefore are a source of heat, so the module is isolated from them with plastic washers. The screw is in contact with the mounting pins, so another plastic washer is used to isolate the module from the screw. The plastic washers raise the module by about 2 mm. This increase in height was enough to cause the lower camera axis to move in its upper limit when performing an autofocus on the sensor, causing the alignment routine to crash. To solve this problem, the entire lower axis of the DSM was moved up a few millimeters so that the upper limit of the axis was at a higher point.

6.2 Cooling Performance

The temperature recorded by the sensors near the stump bridge (sensor 1) and the left edge of the box (sensor 2) during the cold test on the M1805 module is shown as an example in Figure 6.27a. Figure 6.27b shows the temperature measured at the outlet of the heat exchanger during the same period. The temperature in the box drops from 23°C to −10°C over a period of about five hours. At the same time, the temperature in the heat exchanger drops from 22°C to −20°C, resulting in a maximum heat loss of 10°C between the box and the heat exchanger. It takes about 40 minutes to cool the box by 10°C. The cooling time of the box is dominated by the time it takes the heat exchanger to reach sufficiently low temperatures. The measurements are taken during periods of constant temperature. Figure 6.27a shows a small temperature difference between the two locations in the box, indicating a small temperature gradient inside

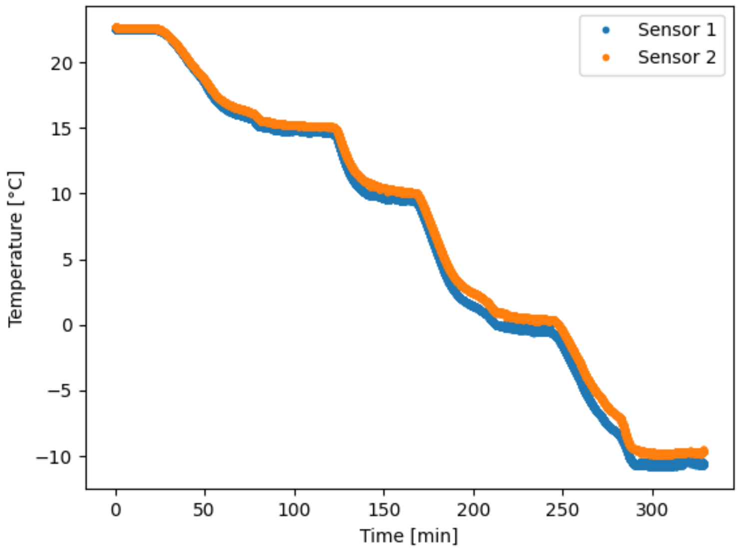

(a) Temperature of both sensors in the box.

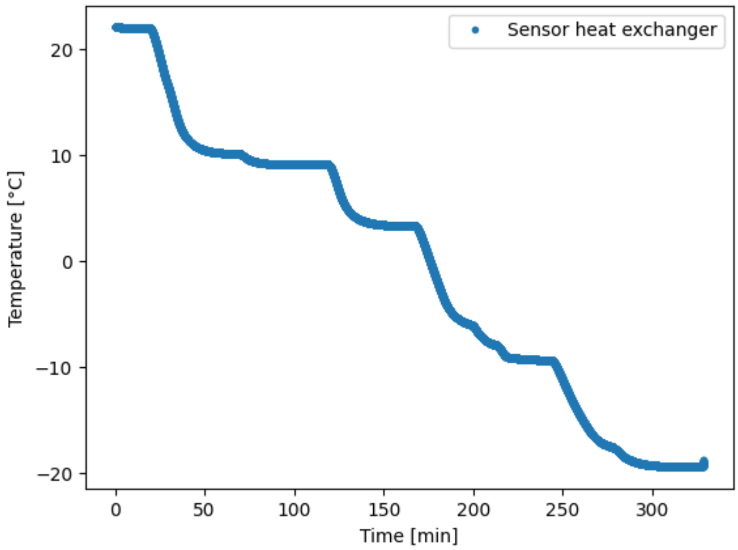

(b) Temperature of the sensor at the exit of the heat exchanger.

Figure 6.27: The measured temperatures of the respective sensors during the cold test of module M1805. The x-axis shows the time in minutes and the y-axis shows the temperature in °C.

the box. The difference is up to 1.4°C, but is less than 1°C during the measurements. After 75 minutes and after 200 minutes, the flow of dry air was increased, increasing the cooling capacity of the setup, visible in Figure 6.27a. However, the airflow was found to have an upper limit, as increasing airflow negatively affects the quality of the measurement of the bottom camera, causing the camera to wiggle. This effect was limited by reducing the amount of dry air coming out of the bottom of the box. The other limiting factor is the power of the cooling machine, which can cool the ethanol to about −23°C. With the given limitations, meaningful measurements can be made up to a temperature of −10°C.

6.3 Cold Test of Module M1805

The cold test performed on module M1805 is exemplarily presented. The alignment of the module was measured at four temperatures. Table 6.9 summarizes the measurements and Figure 6.28 illustrates the results. The statistical and systematical uncertainties are defined in Section 4. The rotation and the translation parallel to the strips show no clear systematic. The absolute rotation between the sensors increases from 23°C to 0°C but decreases again from 0°C to −10°C within the statistical fluctuations. The absolute value of the displacement parallel to the strips increases from 23°C to 10°C but shows no significant change for lower temperatures. The absolute translation perpendicular to the strips strictly decreases and indicates a linear dependence on the temperature. A linear fit results in a slope of:

$$a_{\mathrm{M1805}} \approx (-0.034 \pm 0.002)\,\frac{\mu\mathrm{m}}{^\circ\mathrm{C}}.$$

The fit is additionally depicted in Figure 6.28b. The sign of the slope is inverse to what the plot indicates because of the temperature axis being flipped.
Section 7 will provide more interpretation of the results.

Temperature [°C]	22	10	0	−10
ϕ [µrad]	$-42 \pm 3\,stat. \pm 4\,syst.$	$-46 \pm 3\,stat. \pm 4\,syst.$	$-50 \pm 3\,stat. \pm 4\,syst.$	$-47 \pm 3\,stat. \pm 4\,syst.$
Δx [µm]	$-5.8 \pm 0.1\,stat. \pm 2.2\,syst.$	$-5.4 \pm 0.1\,stat. \pm 2.2\,syst.$	$-5.1 \pm 0.1\,stat. \pm 2.2\,syst.$	$-4.7 \pm 0.1\,stat. \pm 2.2\,syst.$
Δy [µm]	$-6.0 \pm 0.2\,stat. \pm 2.2\,syst.$	$-6.8 \pm 0.2\,stat. \pm 2.2\,syst.$	$-6.9 \pm 0.2\,stat. \pm 2.2\,syst.$	$-6.6 \pm 0.2\,stat. \pm 2.2\,syst.$

Table 6.9: The results of the alignment measurements of module M1805 at four temperatures. The uncertainties are taken from Section 4.

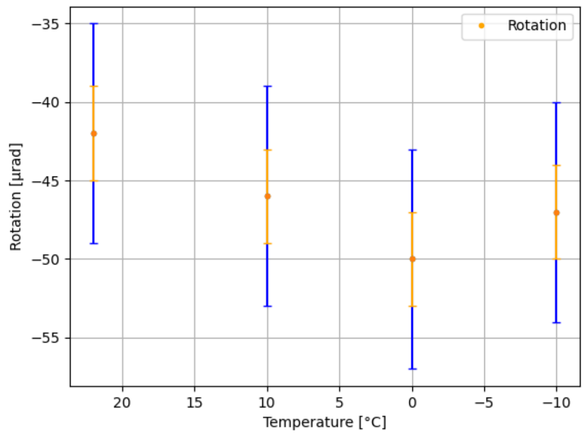

(a) Rotation of module M1805 vs. temperature.

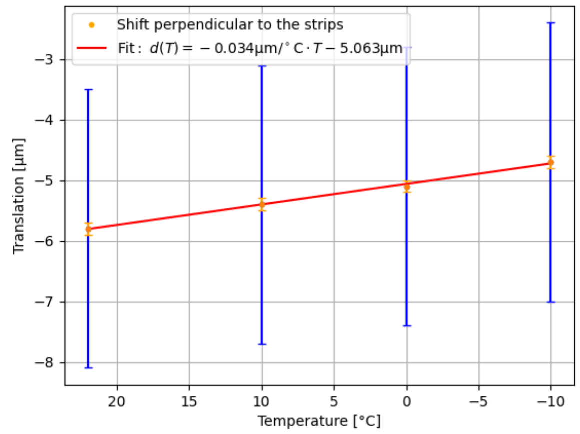

(b) Displacement of the top sensor with respect to the bottom sensor perpendicular to the strips of module M1805 vs. temperature.

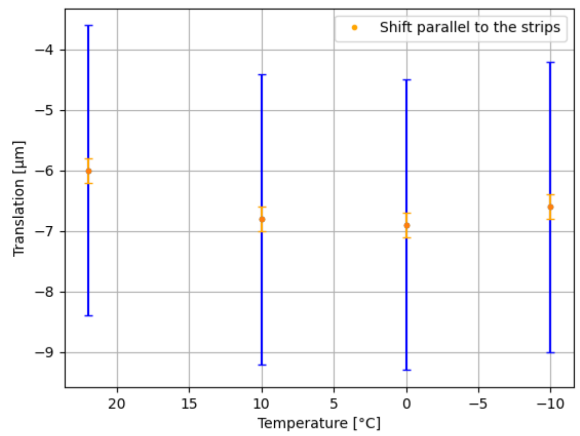

(c) Displacement of the top sensor with respect to the bottom sensor parallel to the strips of module M1805 vs. temperature.

Figure 6.28: Exemplary cold test results of module M1805 at four temperatures down to −10°C.

7 Alignment Measurement Results of Multiple Modules

This chapter summarizes the results of the alignment measurements performed on different modules throughout this work. This includes results of both alignment measurements at room temperature and alignment tests at low temperatures down to $-10°C$, using the setup described in Section 6. The results at room temperature are presented first, followed by the cold test results.

7.1 Alignment Results of Seven Modules

The relative orientation of the silicon sensors of a total of five 1.8 mm modules and two 4 mm modules has been measured during this work. One of the 4 mm modules is a dummy module, which is a module built from sensors that do not provide the electrical readout. The results are summarized in Table 7.10.

The signs of all translational shifts are the same. On average, the shift perpendicular to the strips, Δx, of all 1.8 mm modules is about $-5.5\,\mu m$. Also, the Δx results of both 4 mm modules are close to $-2.2\,\mu m$. The translation perpendicular to the strips of the 4 mm modules tend to be slightly less than for the 1.8 mm modules. Only the shift parallel to the strips, Δy, of the module M1803 and the dummy module are as low as $-2.7\,\mu m$ and $-3.8\,\mu m$, while the rest ranges around $-10\,\mu m$. The rotational shifts of five modules fluctuate around $+36\,\mu rad$, while the angles of two modules differ from the mean by about $\pm 70\,\mu rad$.

All of the presented modules were assembled in the same sensor gluing jig. During assembly, a visual inspection ensured that the edges of the upper and lower sensor both are in contact with the alignment pins of the sensor gluing jig. This exact assembly procedure could explain the observed systematics in the alignment results. The sensor edges parallel to the strips are pushed against two alignment pins, while the edges perpendicular to the strips are pushed against one. Therefore, the modules can be aligned better in the x-direction. This can be seen in the results of all 1.8 mm and 4 mm modules, differing at most 1.1 µm from the respective mean. Although considering the higher uncertainties of the rotational shift, the higher variation of the ϕ results indicates that the assembly procedure is less precise in terms of the rotational alignment.

However, all shifts of the modules are far below the precision requirements of:

$$\Delta x < 50\,\mu m, \quad \Delta y < 100\,\mu m \quad \text{and} \quad \phi < 400\,\mu rad,$$

confirming that the gluing jig setup is suited for the assembly of 2S modules for the Phase-2 Tracker Upgrade.

Module	Δx [µm]	Δy [µm]	ϕ [µrad]
M1802	$-4.9 \pm 0.1\,stat. \pm 2.2\,syst.$	$-8.0 \pm 0.2\,stat. \pm 2.2\,syst.$	$26 \pm 3\,stat. \pm 4\,syst.$
M1803	$-5.0 \pm 0.1\,stat. \pm 2.2\,syst.$	$-2.7 \pm 0.2\,stat. \pm 2.2\,syst.$	$19 \pm 3\,stat. \pm 4\,syst.$
M1804	$-6.6 \pm 0.1\,stat. \pm 2.2\,syst.$	$-12.1 \pm 0.2\,stat. \pm 2.2\,syst.$	$25 \pm 3\,stat. \pm 4\,syst.$
M1805	$-6.4 \pm 0.1\,stat. \pm 2.2\,syst.$	$-7.9 \pm 0.2\,stat. \pm 2.2\,syst.$	$-36 \pm 3\,stat. \pm 4\,syst.$
M1806	$-4.8 \pm 0.1\,stat. \pm 2.2\,syst.$	$-8.3 \pm 0.2\,stat. \pm 2.2\,syst.$	$58 \pm 3\,stat. \pm 4\,syst.$
M4002	$-2.9 \pm 0.1\,stat. \pm 2.2\,syst.$	$-9.9 \pm 0.2\,stat. \pm 2.2\,syst.$	$53 \pm 3\,stat. \pm 4\,syst.$
4 mm Dummy	$-1.5 \pm 0.1\,stat. \pm 2.2\,syst.$	$-3.8 \pm 0.2\,stat. \pm 2.2\,syst.$	$106 \pm 3\,stat. \pm 4\,syst.$

Table 7.10: Combined results of alignment measurements of seven different modules.

7.2 Cold Test Results of Five Modules

Cold tests have been performed on the modules M1802 (Figure 7.29a), M1803 (Figure 7.30a), M1804 (Figure 7.30b), M1805, and M4002 (Figure 7.29b). Module M1802 was the only bare module, and all other modules had their readout electronics already attached. The results of the tests on module M1805 are presented in Section 6.

The results generally differ from the ones in the previous section since they were recorded in the cold test setup. Due to height differences of the module induced by the plastic washers that are used to insulate the module from the mounting pins thermally, different results are expected because a tilted module leads to different results (see Section 4). The statistical and systematical uncertainties in result plots correspond to the uncertainties defined in Section 4. Since the module is not remounted between each measurement, only the statistical uncertainties have to be taken into account when assessing the significance of any effect. However, the systematical uncertainty plays a role in the absolute measured values.

The results show no dependence of the rotation on the temperature within the statistical uncertainties.

Many of the translational displacement results indicate linear effects depending on the temperature. For this reason, linear fits for the displacement in both directions are performed for all modules. The resulting slopes are summarized in Table 7.11. If the slope is significant and much bigger than the corresponding error, the temperature has a significant effect. Four out of the five tested modules show a temperature effect on the shift perpendicular to the strips, while an effect on the displacement parallel to the strips is significant for three modules. At least one of both translational directions is affected by temperature for all modules. The absolute value of the x-displacement decreases for modules M1802 and M1805 and increases for modules M1804 and M4002. The absolute value of the y-displacement decreases for module M1804 and increases for modules M1803 and M4002.

With both modules M1804 and M1803 another measurement was recorded at room temperature after the cooling to $-10°$C in order to check if the changes of the shifts are elastic, so they would return to the same value at room temperature before cooling. The green crosses in Figure 7.30 indicate the results of these measurements. The measurements agree within $1\sigma_{stat}$ except for the displacement perpendicular to the strips of the module M1803, which agrees within $2\sigma_{stat}$ of the measurements recorded before cooling.

Module	$a_{\Delta x}$ [μm/°C]	$a_{\Delta y}$ [μm/°C]
M1802	-0.061 ± 0.009	0.006 ± 0.008
M1803	0.006 ± 0.009	0.044 ± 0.007
M1804	0.023 ± 0.005	-0.032 ± 0.006
M1805	-0.034 ± 0.002	0.019 ± 0.016
M4002	0.075 ± 0.019	0.041 ± 0.009

Table 7.11: The slopes resulting from fitting a straight line to the results of all translational displacements.

To compare the magnitude of the change in the shifts, the results are shown relative to the measurement at 22°C in Figure 7.31. Although the displacement perpendicular to the strips of module M4002 is affected the most by temperature, it is not much bigger than the effect on the other shifts.

To further emphasize the differences in the size of temperature effects on the displacement between each module, the absolute translational shift is computed from the shifts in the x-direction and the y-direction:

$$d = \sqrt{\Delta x^2 + \Delta y^2}.$$

These shifts are depicted against the temperature for all modules relative to the 22°C measurement in Figure 7.32. It can be seen that the temperature effects are all in the same order of magnitude.

As a result of the tests, it can be said that all measured shifts with the temperature are too small to have any negative impact on things like the stub finding logic. The limits on Δx are more stringent than the Δy limits. Even the greatest measured change of Δx of 0.075 μm/°C is not problematic. Over a temperature range 60°C, representing the temperature difference between room temperature ($\approx$ 25°C) and the temperature of the CO_2 of the CMS Phase-2 Tracker (≈ -35°C), Δx changes by 4.5 μm, assuming the validity of the linear dependence. This is much smaller than the precision requirement of $\Delta x < 50$ μm. The sensor-to-sensor alignment is not expected to depend strongly on temperature since the coefficients of thermal expansion of the silicon sensors and the spacers are nearly the same (see Section 2.3.1). Another conclusion is that during serial production, measurements can be recorded at room temperature, and the results are still valid at temperatures of -35°C.

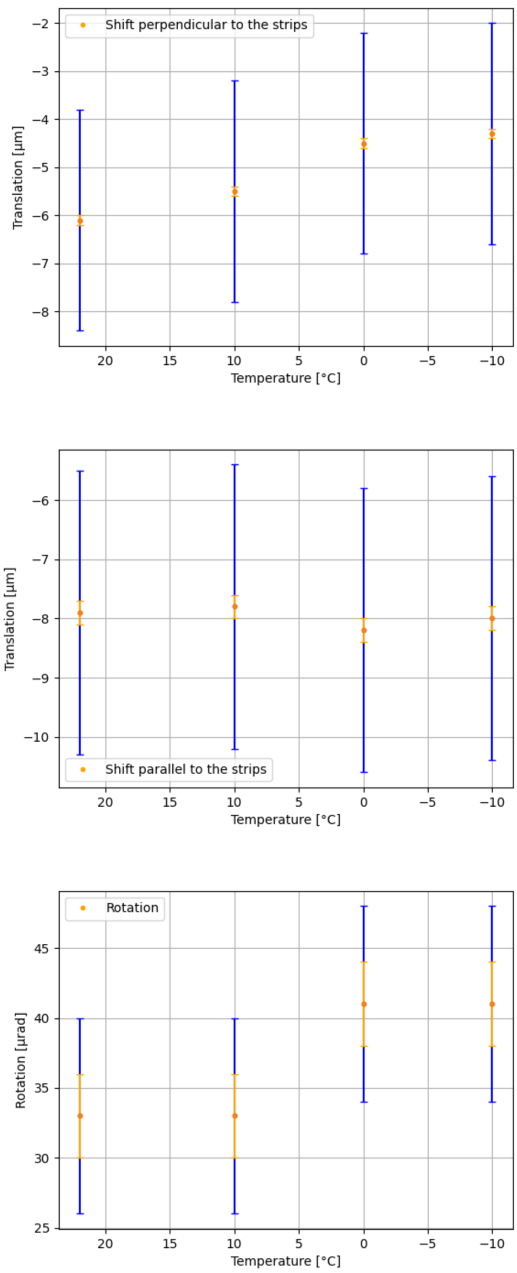

(a) Module M1802

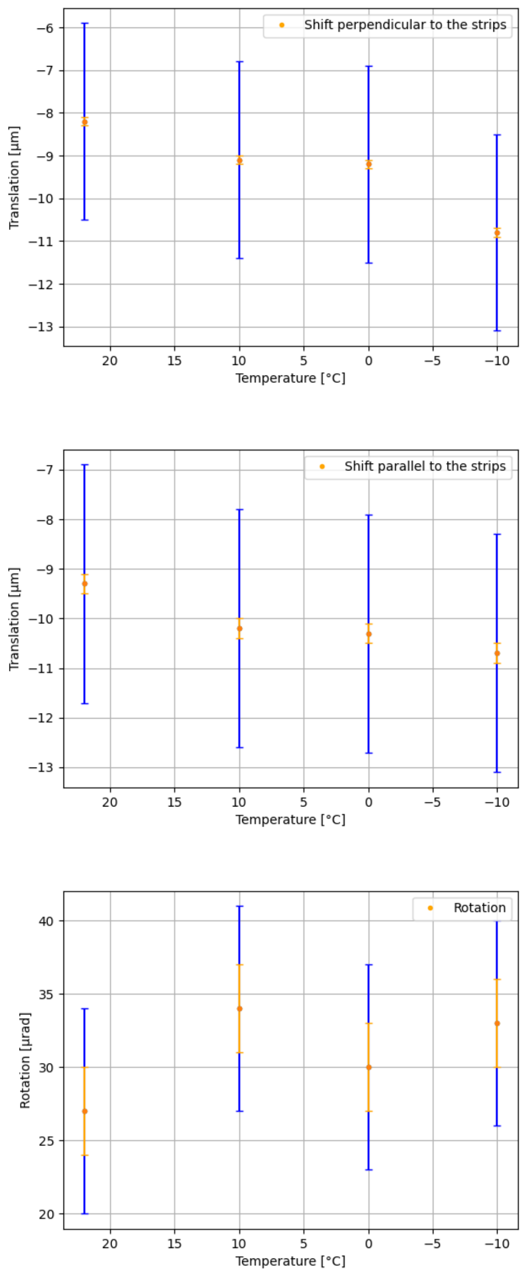

(b) Module M4002

Figure 7.29: The results of the cold tests of modules M1805 (left) and M4002 (right). The orange points are the respective measurement results, the orange error bars represent the statistical uncertainties, and the blue bars are the systematical uncertainties.

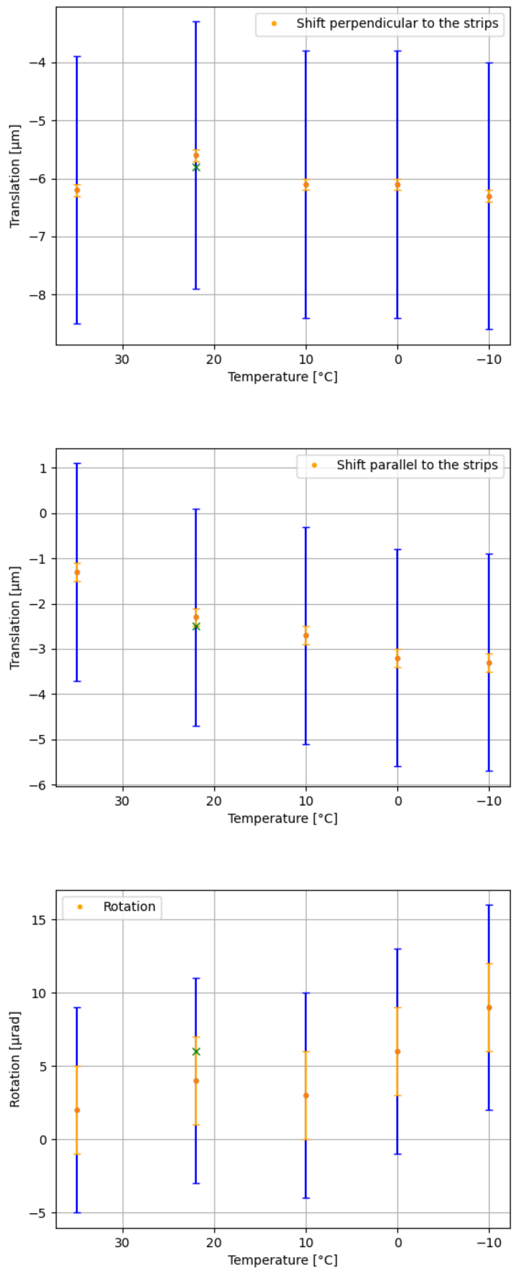

(a) Module M1803

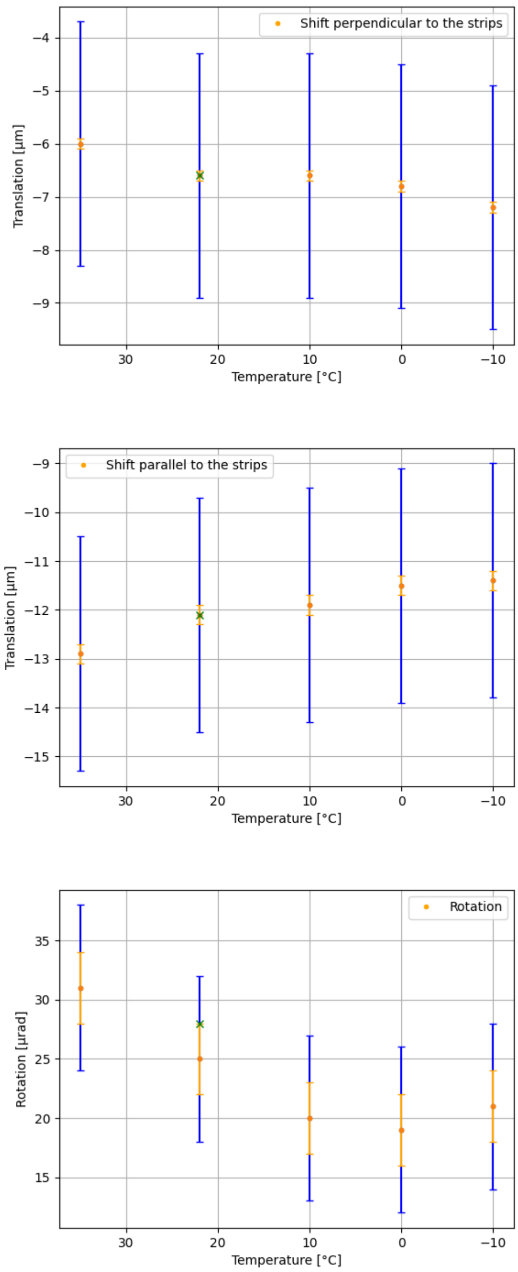

(b) Module M1804

Figure 7.30: The results of the cold tests of the modules M1803 (left) and M1804 (right). The orange points are the respective measurement results, the orange error bars represent the statistical uncertainties and the blue bars are the systematical uncertainties. The green cross represents the results of the measurement recorded after the cooling to $-10°C$.

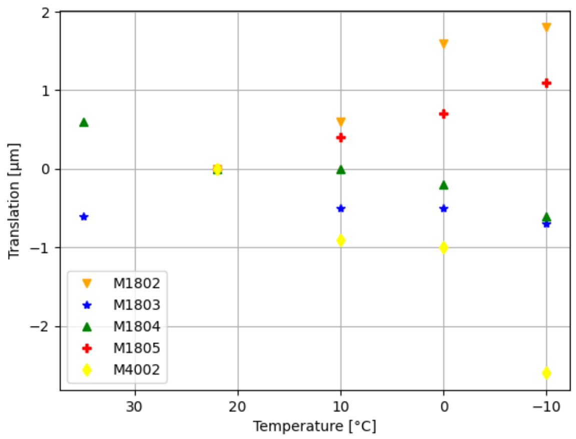

(a) Translation perpendicular to the strips vs. temperature.

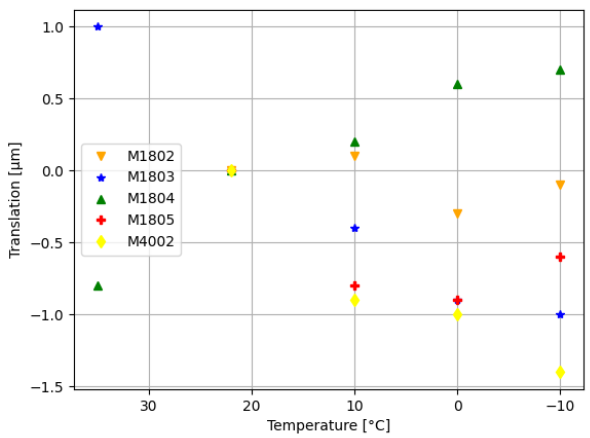

(b) Translation parallel to the strips vs. temperature.

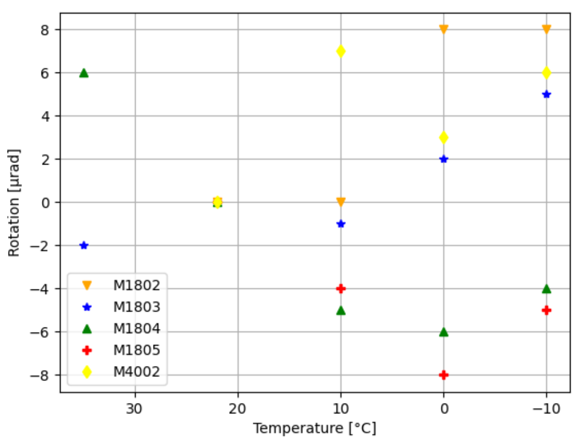

(c) Rotation vs. temperature.

Figure 7.31: Combined cold test results relative to the measurement at 22°C.

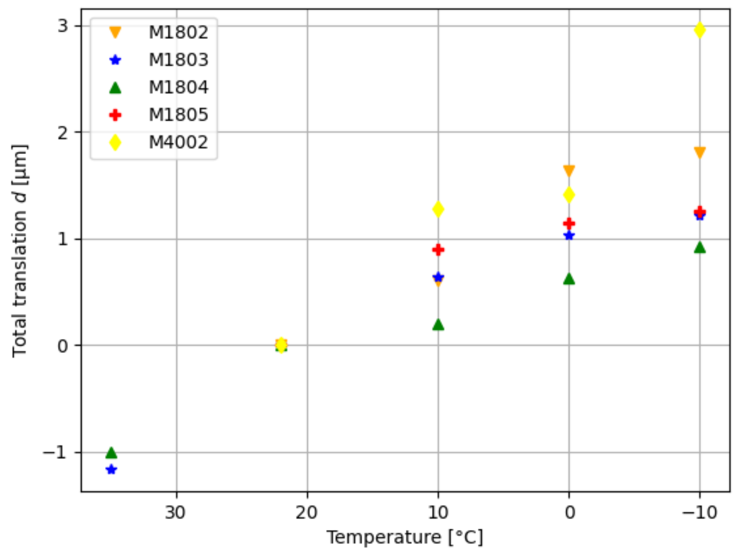

Figure 7.32: The absolute translational shift relative to the 22°C measurement for all modules.

7.3 Alignment Measurement with a Thermally Cycled Module

The cold tests of this work were completed with a measurement, testing if a module cooled to lower temperatures than −10°C would still show elastic expansion. For that, a climate chamber was used, which is capable of reaching lower temperatures than the cold test setup. Module M1802 was cycled in the climate chamber between +35°C and −35°C for a total of ten times, out of which the temperature was held at −35°C twice for 30 minutes. The temperature of −35°C was chosen to simulate the temperature in the Outer Tracker as close as possible, while +35°C was the highest temperature reached in the cold test setup. Alignment measurements were recorded before and after the thermal cycling:

$$\Delta x_{\text{before}} = (-4.4 \pm 0.1\, stat. \pm 2.2\, syst.)\ \mu\text{m}$$
$$\Delta y_{\text{before}} = (-7.7 \pm 0.2\, stat. \pm 2.2\, syst.)\ \mu\text{m}$$
$$\phi_{\text{before}} = (32 \pm 3\, stat. \pm 4\, syst.)\ \mu\text{rad},$$

and

$$\Delta x_{\text{after}} = (-4.5 \pm 0.1\, stat. \pm 2.2\, syst.)\ \mu\text{m}$$
$$\Delta y_{\text{after}} = (-7.8 \pm 0.2\, stat. \pm 2.2\, syst.)\ \mu\text{m}$$
$$\phi_{\text{after}} = (30 \pm 3\, stat. \pm 4\, syst.)\ \mu\text{rad}.$$

The results are almost identical, giving no indication of inelastic shifts depending on temperature down to −35°C.

8 Sensor-Bridge Alignment

Besides the relative alignment of the sensors to each other, the alignment of the spacers and the stump bridges relative to the upper and lower sensors is also of interest. The measurement could provide information about possible systematic misalignments that occur during assembly. The sensor-bridge alignment routine was developed for this purpose. This section introduces the measurement idea and the measurement routine and presents an example result.

8.1 The Basic Principle

The bare modules are assembled in the sensor gluing jig. Due to tolerances in the assembly of the bare module, the spacers, the stump bridges, and the two silicon sensors are most likely not aligned to each other as they should be according to the construction plan of a 2S module. Even if both sensors are well aligned, the holes of the spacers might be tilted relative to the sensors. This can be a problem because the holes may not fit on the cooling structure. With the sensor-to-sensor alignment measurement, this cannot be noticed.
The pattern recognition developed for the sensor-to-sensor alignment measurement can be used to determine the exact position of the sensor in the cameras. The position at which the spacer holes should be located relative to this sensor position can be determined from the module design drawings. The offset between the nominal position of the holes and their actual position reflects the orientation between the spacers and the sensor. In the same manner, the orientation between the stump bridges and the sensors can be determined. The measurement of this offset is the basic idea of the routine.
The image size of the cameras is too small to capture an image of the entire holes in the spacers. Therefore, the edges of the holes are used as a distinguishing feature between the nominal position of the holes and the actual position. Based on the nominal position of the holes and their nominal radius, the location where the edges of the holes should be can be represented by circles. Taking an image of the actual edge of a hole and displaying the norm position of the respective hole in the same picture, the offset can be determined from the image by the user (Figure 8.33).
In the DSM setup, only the upper camera can take an image of the vicinity of the holes since the view of the lower camera is obstructed by the mounting pins. This means that only the alignment between the upper sensor and the spacers and the stump bridges can be measured. However, this is sufficient because the orientation of the upper sensor to the lower sensor is measured with the alignment routine. The combination of the measurements results in the orientation of the lower sensor to the spacers and the stump bridges.
As the actual positions of the holes are determined, the sensor-bridge alignment routine is also used to determine the precision of the position of the holes with respect to each other.

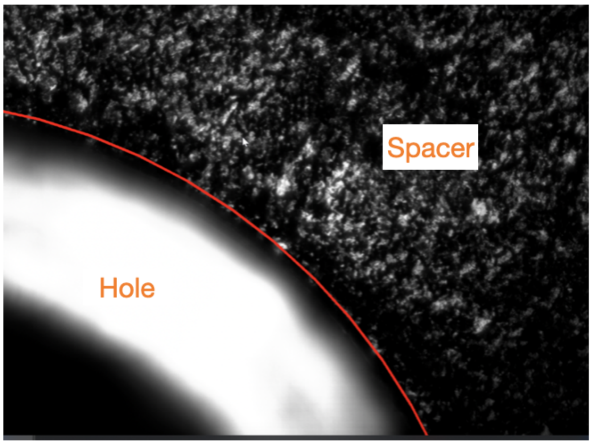

Figure 8.33: An example picture taken of the portion of a hole in a 2S module spacer (dark grey area), together with the nominal position of the same portion of the hole indicated as a red circle. The blurred part in the lower left is the mounting pin of the DSM setup. The depth of field is 15 µm (Section 3.2).

8.2 The Measurement

The sensor-bridge alignment routine is developed as a follow-up measurement of a sensor-to-sensor alignment test. When the analysis of a sensor-to-sensor alignment measurement is run from the GUI, the user has the option to measure the sensor-bridge alignment after the analysis is complete. Figure 8.34 shows the part of the graphical user interface used for monitoring the measurement. The "Get Transformation" button is activated after an alignment measurement has been evaluated. Clicking the button causes the xy-table and the upper camera to move to the first measurement position defined in the configuration for the sensor-to-sensor alignment measurement. The camera performs an autofocus and captures an image of the upper sensor, which is stored. This process is repeated at the second measurement position. These images are used to determine the exact position of the sensor in the camera. The pattern recognition of the sensor-to-sensor alignment routine is applied to the first image to define the transformation of the sensor to the camera at that point.
The second measurement is needed to define the angle between the sensor and the xy-stage. By design, the exact sensor position at the first point, the exact sensor position at the second point, and the expected sensor position at the second point, assuming no rotation, form an isosceles triangle (Figure 8.35). The difference between the expected position and the actual position at the second point is the offset caused by a sensor rotation with respect to the xy-stage. The opening angle of the triangle is calculated from this difference and the distance traveled by the table. To do so, the x-distance of the table must be converted to pixels. The scaling factor used is the average of the scaling factors defined for the images at the two measurement points.

The opening angle of the triangle can be used to calculate the offset resulting from the rotation of the sensor with respect to the measuring stage at each point. Using the properties of isosceles triangles and trigonometric correlations, the offsets depending on the distance Δx

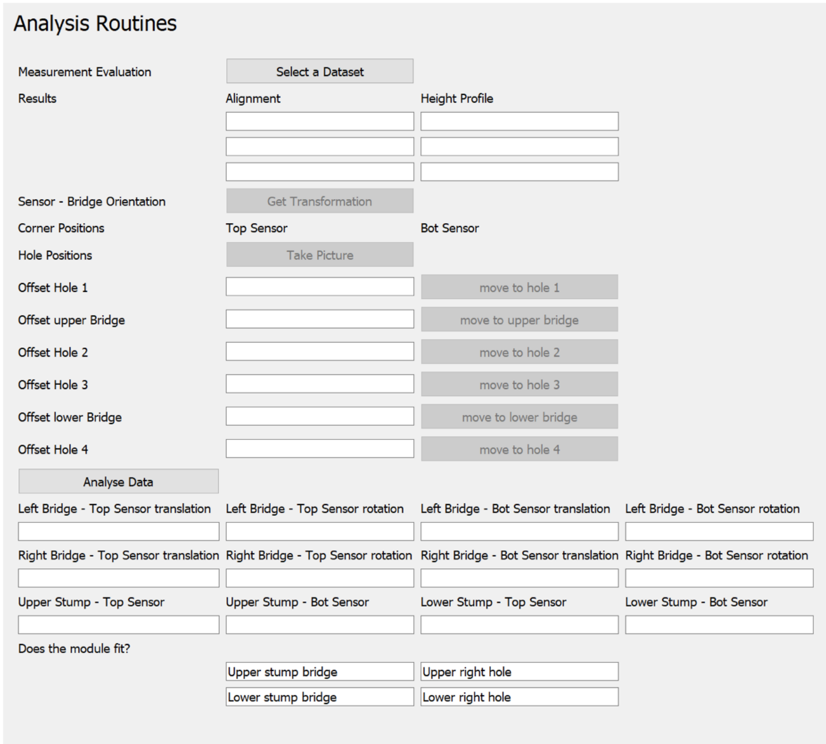

Figure 8.34: A screenshot of the part of the GUI that is used for the sensor-bridge alignment. The individual buttons and their functions are explained in the text.

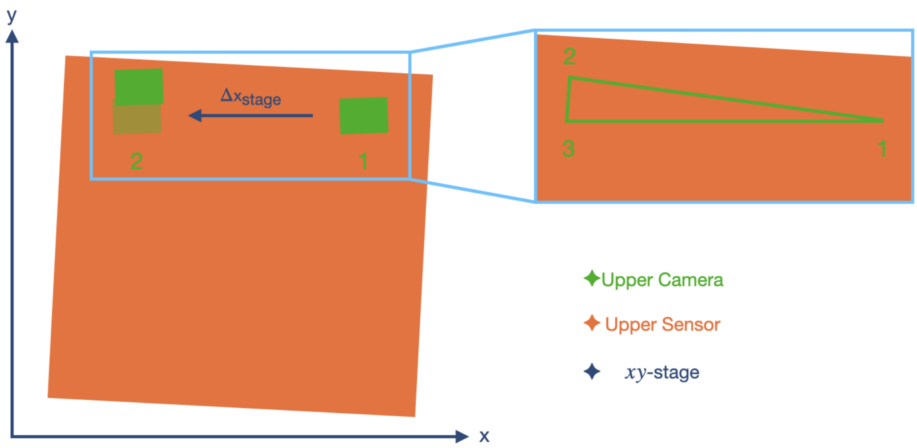

Figure 8.35: A sketch of the module in the DSM. The orange area represents the upper sensor. The green rectangles illustrate the field of view of the upper camera. The x- and y-axes of the stage and the x-distance moved to get from the first measurement point to the second are shown in dark blue. The view on the area boxed in light blue indicates the triangle that is spanned by the first measurement point, the second measurement point, and the point that results from using the transformation defined at the first point on the second point.

traveled in the x-direction of the table are:

$$\Delta a = 2\Delta x \cdot sin\left(\frac{\gamma}{2}\right)^2$$
$$\Delta b = 2\Delta x \cdot sin\left(\frac{\gamma}{2}\right) cos\left(\frac{\gamma}{2}\right),$$

where Δa is the offset in the x-direction, Δb is the offset in the y-direction, and γ is the opening angle computed before. Since the sensors are built with 90° angles in the corners, an offset depending on the y-distance moved away from the first measurement point arises due to the same logic. This offset is symmetric to the first and results in the following additional shifts in the camera:

$$\Delta a' = 2\Delta y \cdot sin\left(\frac{\gamma}{2}\right) cos\left(\frac{\gamma}{2}\right)$$
$$\Delta b' = 2\Delta y \cdot sin\left(\frac{\gamma}{2}\right)^2,$$

where Δy is the y-distance of any point on the sensor to the first measurement point. The total offset is the sum of both individual offsets:

$$\Delta a_{\text{tot}} = \Delta a + \Delta a'$$
$$\Delta b_{\text{tot}} = \Delta b + \Delta b'.$$

Once the transformations are defined, and the γ angle is calculated, all buttons of the sensor bridge alignment routine are enabled.
The button "move to hole 1" causes the xy-stage to move to the upper edge of the upper left hole of the module. The user must look at the live image in the GUI to see if there is a clear image of the edge. If not, the user must manually move the xy-stage and the z-axis of the top camera. Clicking the "Take Picture" button will save the image currently visible in the GUI. This picture will then open in a pop-up window showing the nominal edge of the hole in red (Figure 8.36). To account for the distance between the position where the image was taken and the position of the center of the nominal circle, the xy-position of the table at the time of the acquisition is also stored. The difference between these two positions is the final displacement that must be taken into account in order to display the nominal circle at the correct position.

In the pop-up window, the user has to measure the y-offset between the nominal position and the actual hole position by clicking on the highest point of the red circle first and on the highest point of the actual sensor edge afterwards. The xy-positions of both clicks are displayed as blue numbers in pixels. Pressing any button on the keyboard closes the pop-up window and calculates the offset between the y values of both click positions in micrometers. In the next step, the user has to manually move the stage such that the right side of the hole is visible clearly in the GUI. Pushing the "Take Picture" button again opens the pop-up window with the current image and plots in the nominal hole edge for a x-offset measurement. This time, the user clicks on the rightmost point of the circle and the rightmost point on the real hole, and the routine computes the x-offset in micrometers. The "Take Picture" button is coded

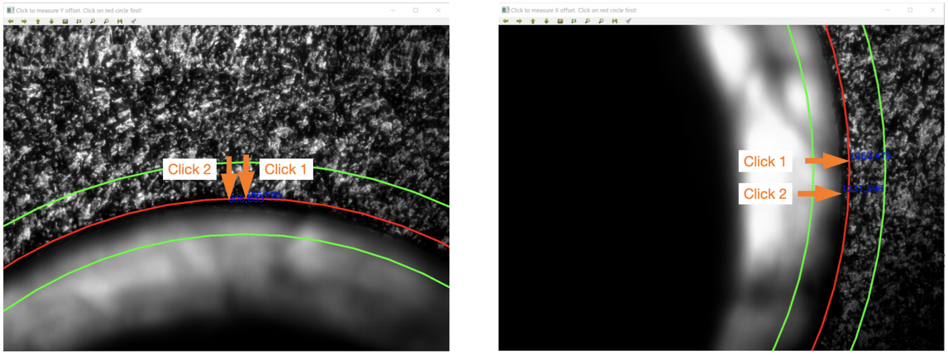

Figure 8.36: Examples of pop-up windows for a y-offset measurement (left) and a x-offset measurement (right). The red circle represents the nominal hole edge. The green circles indicate a ±100 µm big interval around the nominal radius. The orange arrows represent the positions of the clicks of the user. The blue numbers are x- and y-coordinates of the click positions in pixels.

to alternate between an expected y-offset and x-offset measurement, starting with a y-offset measurement after an alignment analysis.
The user repeats the steps of measuring the offsets at all other holes. The routine has the information which hole is currently investigated by computing the difference between the current stage position and the stage position of every hole. The hole to which the distance is minimal is the currently tested hole, and the routine automatically prints the results into the text box corresponding to that hole. This means that the user can probe the holes in any order. The upper left hole is referred to as "hole 1", "hole 2" is the upper right hole, "hole 3" is the one in the lower right, and "hole 4" is the lower left hole.
Once all offsets are measured, the "Analyse Data" button is clicked to determine the xy-stage coordinates of the actual holes and compute the final results. The offsets of the stump bridges are a measure of the translational shift between the stump bridges and the sensor. For the left spacer, a line is calculated using the corresponding holes (Figure 8.37).

Another line is computed between the upper left and lower left corners of the sensor. The angle under which these lines intersect is used as a measure of the rotational shift of the spacer to the sensor. The translational shift is defined as the xy-difference of the points in the middle of the lines. The nominal xy-difference of these points has to be subtracted since regarded points do not lie over each other by construction. These shifts are computed for the right spacer and the right edge of the sensor as well. All shifts are also computed with respect to the lower sensor analogously by determining the position of the lower sensor using the transformation from upper to lower sensor defined at the end of the sensor-to-sensor alignment analysis. All results are displayed in the corresponding text boxes shown in Figure 8.34. The results are computed in xy-stage coordinates so that the positive x-axis points to the right and the positive y-axis points to the back of the DSM.
Additionally, it is checked if the distances of the holes relative to each other meet the requirement to not differ more than 100 µm [5] from the nominal distance given in the construction

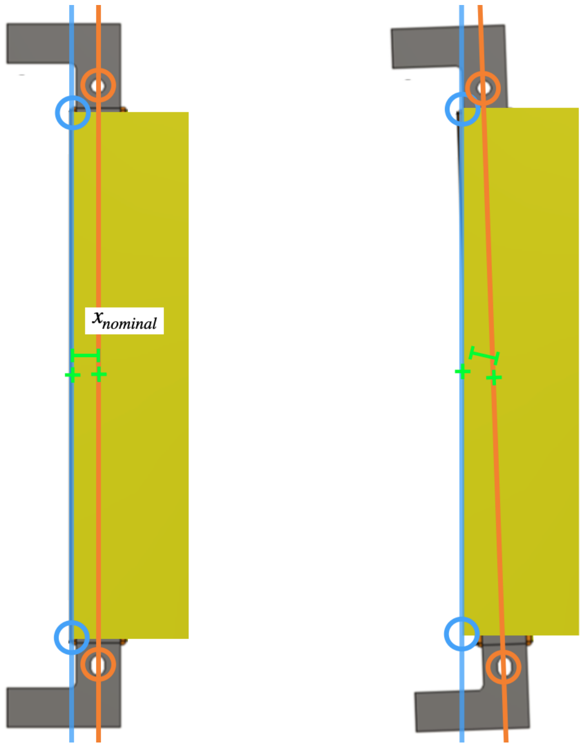

Figure 8.37: The scheme of the left spacer and a portion of the upper sensor (yellow). On the left, a module with a perfect sensor-bridge alignment is illustrated. On the right, the spacer is tilted and shifted with respect to the upper sensor. The blue circles respectively indicate the positions used for calculating a straight line (blue line) through the sensor edges. The line through the spacer holes is shown in orange. The green crosses indicate the positions used for calculating the translational shift. In the left picture, the nominal x-shift of 4.85 mm is displayed to illustrate that the nominal shift has to be subtracted for a real module. The angle under which the lines in the right picture intersect is the rotational difference of the bridge with respect to the sensor.

plan. This test ensures that the module can be screwed to the support structure. If the module is built perfectly, the holes form a rectangle. A large offset of one spacer does not necessarily mean that the module cannot fit. The other holes could be shifted in the same direction, such that the rectangle is preserved.
The idea for the test is sketched in Figure 8.38. The slope of the line through the holes of the left spacer is used to construct two lines pointing to the right at a 90° angle with respect to the line through the holes. One of those constructed lines originates at the upper left hole position, and the other starts at the lower left hole position. If the module is built perfectly rectangular, the positions of the upper stump bridge hole and the upper right hole are expected to be on the line starting at the upper left hole. These expected positions on the line can be computed using the nominal distances between the holes. Likewise, the lower stump bridge and the lower right hole are expected to lie on the line starting at the lower left hole. With the true positions being known, the difference between the expected and the real position can be calculated. This difference must be smaller than 100 μm to meet the requirements. The text boxes at the bottom of Figure 8.34 show if the condition is met at the corresponding position by turning green if they do and turning red if they do not.

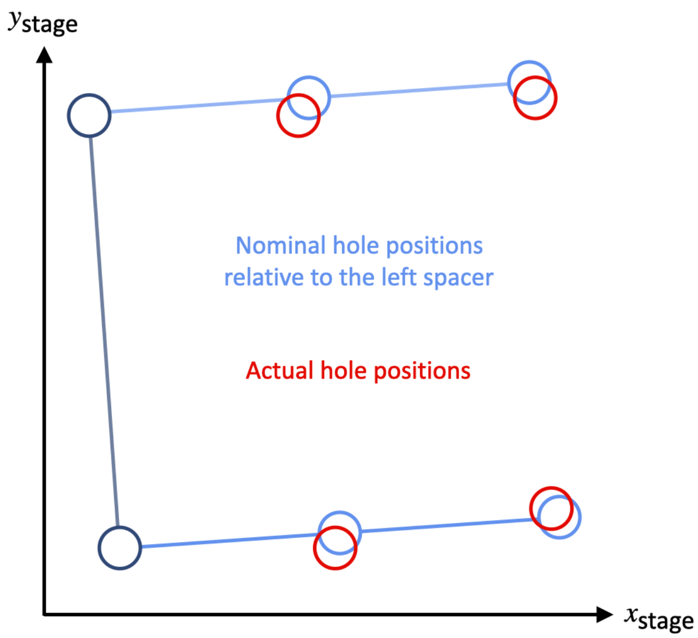

Figure 8.38: A sketch illustrating the measurement of the precision of the hole positions with respect to each other. The light blue lines indicate the line on which the holes should be if the module is built perfectly rectangular with respect to the left spacer. The left spacer and its holes are represented in dark blue.

8.3 Example Sensor-Bridge Alignment Measurement

As a test of the routine, the sensor-bridge alignment of module M1805 has been measured. The results in Figure 8.39 show no offset exceeding any precision requirements.

To check if the results of the routine are reproducible, the offsets of module M1805 have been measured six times. The results are summarized in Table 8.12.

The order of magnitude of the offsets can always be reproduced, but it can be observed that the variation of the results is different for different holes. For example, the x-offsets for hole 2 range from $-20.19\,\mu\text{m}$ up to $-32.63\,\mu\text{m}$ while the x-offsets of the upper stump bridge lie between $-1.55\,\mu\text{m}$ and $0.0\,\mu\text{m}$. This is due to the holes showing variance in the roundness of the edges of the hole. As a consequence, it is challenging for the user to decide which point of the real hole is the highest in the case of a y-offset measurement or which point is the rightmost in the case of a x-offset measurement. Therefore, the highest uncertainty of Table 8.12, rounded to the first significant digit, is used as an estimate of the uncertainty for an offset measurement:

$$\sigma \approx 5\,\mu\text{m}.$$

The most significant offsets at hole 2 and hole 4 have been measured in another way to see if the results from the sensor-bridge alignment routine can be confirmed. This was done by manually searching for the respective hole position in the xy-stage. By moving the xy-stage and the upper camera to the upper edge of the respective hole and then to the lower edge, noting both y-positions, the y-coordinate of the center of the hole can be determined by computing the mean of both values. Likewise, the x-coordinates of both holes are determined. Afterwards, the stage is moved so that the middle of an alignment marker is centered in the camera to measure xy-coordinates of that marker on the sensor. Deviations of the nominal distances from that marker to the respective holes are a measure of the same offset measured in the sensor-bridge alignment. The results for hole 2 are:

$$x = -24\,\mu\text{m} \quad \text{and} \quad y = -8\,\mu\text{m},$$

Measurement	1	2	3	4	5	6	Mean	σ
Hole 1 offsets	$x = -5.44\,\mu\text{m}$ $y = 0.0\,\mu\text{m}$	$x = -3.11\,\mu\text{m}$ $y = -4.66\,\mu\text{m}$	$x = -0.78\,\mu\text{m}$ $y = 2.33\,\mu\text{m}$	$x = 0.0\,\mu\text{m}$ $y = -0.78\,\mu\text{m}$	$x = -4.66\,\mu\text{m}$ $y = 0.78\,\mu\text{m}$	$x = -3.11\,\mu\text{m}$ $y = 1.55\,\mu\text{m}$	$\bar{x} = -2.85\,\mu\text{m}$ $\bar{y} = -0.13\,\mu\text{m}$	$\sigma_x = 2.12\,\mu\text{m}$ $\sigma_y = 2.48\,\mu\text{m}$
Hole 2 offsets	$x = -21.74\,\mu\text{m}$ $y = -6.21\,\mu\text{m}$	$x = -30.31\,\mu\text{m}$ $y = -6.22\,\mu\text{m}$	$x = -26.39\,\mu\text{m}$ $y = -10.09\,\mu\text{m}$	$x = -31.63\,\mu\text{m}$ $y = -8.55\,\mu\text{m}$	$x = -20.19\,\mu\text{m}$ $y = -6.99\,\mu\text{m}$	$x = -24.84\,\mu\text{m}$ $y = -8.54\,\mu\text{m}$	$\bar{x} = -26.02\,\mu\text{m}$ $\bar{y} = -7.77\,\mu\text{m}$	$\sigma_x = 4.82\,\mu\text{m}$ $\sigma_y = 1.55\,\mu\text{m}$
Hole 3 offsets	$x = -11.65\,\mu\text{m}$ $y = 1.55\,\mu\text{m}$	$x = -10.88\,\mu\text{m}$ $y = 2.33\,\mu\text{m}$	$x = -11.64\,\mu\text{m}$ $y = 2.33\,\mu\text{m}$	$x = -11.65\,\mu\text{m}$ $y = -5.44\,\mu\text{m}$	$x = -10.09\,\mu\text{m}$ $y = 1.55\,\mu\text{m}$	$x = -11.64\,\mu\text{m}$ $y = -0.78\,\mu\text{m}$	$\bar{x} = -11.26\,\mu\text{m}$ $\bar{y} = 0.26\,\mu\text{m}$	$\sigma_x = 0.65\,\mu\text{m}$ $\sigma_y = 3.02\,\mu\text{m}$
Hole 4 offsets	$x = -10.87\,\mu\text{m}$ $y = -45.81\,\mu\text{m}$	$x = -16.32\,\mu\text{m}$ $y = -47.40\,\mu\text{m}$	$x = -17.85\,\mu\text{m}$ $y = -43.47\,\mu\text{m}$	$x = -12.43\,\mu\text{m}$ $y = -45.06\,\mu\text{m}$	$x = -16.31\,\mu\text{m}$ $y = -44.26\,\mu\text{m}$	$x = -12.42\,\mu\text{m}$ $y = -48.91\,\mu\text{m}$	$\bar{x} = -14.37\,\mu\text{m}$ $\bar{y} = -45.82\,\mu\text{m}$	$\sigma_x = 2.81\,\mu\text{m}$ $\sigma_y = 2.03\,\mu\text{m}$
Upper bridge offsets	$x = -1.55\,\mu\text{m}$ $y = 10.09\,\mu\text{m}$	$x = -0.78\,\mu\text{m}$ $y = 6.99\,\mu\text{m}$	$x = 0.0\,\mu\text{m}$ $y = 8.54\,\mu\text{m}$	$x = 0.0\,\mu\text{m}$ $y = 8.55\,\mu\text{m}$	$x = -0.78\,\mu\text{m}$ $y = 6.99\,\mu\text{m}$	$x = -1.55\,\mu\text{m}$ $y = 5.43\,\mu\text{m}$	$\bar{x} = -0.78\,\mu\text{m}$ $\bar{y} = 7.77\,\mu\text{m}$	$\sigma_x = 0.70\,\mu\text{m}$ $\sigma_y = 1.63\,\mu\text{m}$

Table 8.12: The results for the offsets of the sensor-bridge alignment routine of six measurements performed on module M1805. The arithmetic average and the root mean square are also computed.

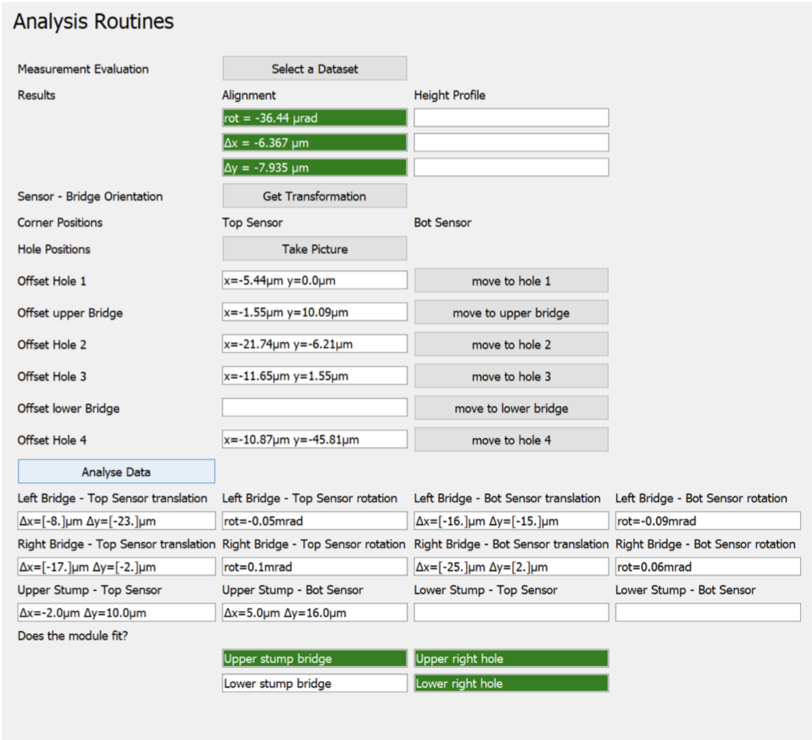

Figure 8.39: A screenshot of the analysis section of the GUI. In the upper text boxes, the alignment results are shown. The offsets resulting from the measurement are displayed in the text boxes in the middle. The final results are shown in the text boxes below. The green-colored text boxes on the bottom indicate that the precision of the hole positions with respect to each other meet the requirements. Since this module is built with only one stump bridge, there are no results in the text boxes for the lower stump bridges.

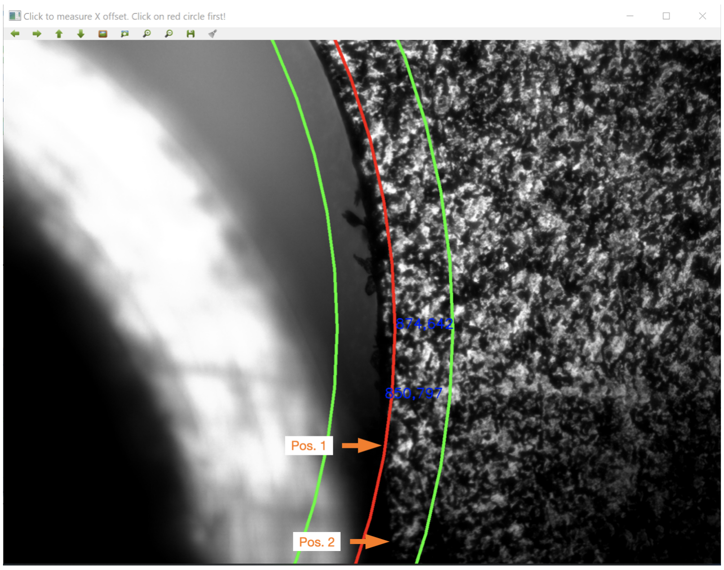

Figure 8.40: The pop-up window for the x-offset measurement at hole 4. "Pos. 1" and "Pos. 2" can both be assumed to be the rightmost position.

and for hole 4:

$$x = -8\,\mu\text{m} \quad \text{and} \quad y = -48\,\mu\text{m}.$$

The means computed for the respective holes from Table 8.12 for hole 2 are:

$$\bar{x} = -26\,\mu\text{m} \quad \text{and} \quad \bar{y} = -8\,\mu\text{m},$$

and for hole 4:

$$\bar{x} = -14\,\mu\text{m} \quad \text{and} \quad \bar{y} = -46\,\mu\text{m}.$$

Comparing the corresponding values shows an agreement between the results of both methods within 1σ except for the x-offset measurement of hole 4 that agrees within 2σ. The validity of the sensor-bridge alignment measurement can be confirmed. The large deviation of 6 µm between the two methods is observed for the x-offset of hole 4, which can be categorized as a hole with a bad rounded edge (Figure 8.40). For the measurements 2, 3, and 5 in Table 8.12, the position chosen to be the rightmost one was in the vicinity of the position indicated as "Pos. 1" in Figure 8.40. In contrast, positions in the direct surrounding of "Pos. 2" in Figure 8.40 have been chosen to be the most right ones for measurements 1, 4, and 6.

9 Conclusion and Outlook

A precise alignment between the sensors of the novel 2S module is mandatory for the functionality of the stub mechanism. In Aachen, a DSM setup is used to measure the relative alignment of the two sensors on a micrometer scale. Prior to this work, the setup could be used for measurements but was not suitable for use in the module production phase.
During the course of this work, several improvements to the DSM machine were introduced regarding the ease of use of the setup.
An analysis of the statistical and systematic measurement uncertainties of the sensor-to-sensor alignment measurement was performed. The results show that the sensor-to-sensor alignment can be measured with a precision of:

$$\sigma_{\Delta x,\text{stat}} = 0.1\,\mu\text{m}, \qquad \sigma_{\Delta y,\text{stat}} = 0.2\,\mu\text{m} \quad \text{and} \quad \sigma_{\phi,\text{stat}} = 3\,\mu\text{rad}.$$

The analysis of the systematical uncertainties showed that the only source of uncertainty is essentially the angle of the sensor surface with respect to the camera. The systematical uncertainty is estimated at:

$$\sigma_{\Delta x,\text{sys}} = 2.2\,\mu\text{m}, \quad \sigma_{\Delta y,\text{sys}} = 2.2\,\mu\text{m} \quad \text{and} \quad \sigma_{\phi,\text{sys}} = 4\,\mu\text{rad}.$$

So far, precision measurements were only possible at room temperature. The DSM setup has been successfully improved so that a module can be cooled down to $-10°$C with cold, dry air in a custom plastic box. Since the top and bottom of the box are sealed with a glass plate, DSM measurements are still possible. Cold tests of five different modules show a trend of translational displacement of the modules with temperature. Taking the largest measured shift per temperature and assuming the validity of the linear temperature dependence, the Δx displacement changes by about 4.5 µm over a temperature interval of 60° C. This is less than 10% of the allowed shift of 50 µm. The rotation between the sensors is not affected by the temperature. The tests show that the effect of temperature on the sensor-to-sensor alignment is minimal and does not negatively affect the stub mechanism. Also, the results show that for serial production, measurements can be recorded at room temperature, and the results are still valid at temperatures in the Outer Tracker.
The sensor-to-sensor alignment results of seven different modules show a clear systematic of always positive rotations and negative translations both in x-direction and in y-direction. The displacement in the x-direction is always about -5.5m for 1.8 mm modules which is almost a factor of 10 better than the required precision. All modules were assembled in the same sensor gluing jig. During assembly, a visual inspection ensured good contact between the sensor edges of both sensors and the jigs alignment pins. This precise assembly could be the reason for the observed systematics. Future modules will be built with a new gluing jig. It should be checked whether the modules built with the new jig also tend to a specific value or not. It is of particular interest to check whether a 1.8 mm module assembled with the new jig measures a value that is very different from -5.5 µm.

Finally, a new alignment method was implemented in the setup allowing measurements of the alignment of the sensors with respect to the spacers. By determining the exact position of the sensor in the camera, the nominal position of the spacer holes can be computed with respect to that sensor position. Deviations of the actual spacer holes from the nominal hole are a measure of the offset. The offsets are measured by displaying the nominal positions of the spacer holes along with the real position in the GUI of the DSM software. The offset is then defined by clicking on the respective positions. This test is ultimately performed because even with a sensor with well-aligned sensors, the spacers may be tilted so much relative to each other that the module will not fit on the CMS cooling structure. The first test with module M1805 shows that all measured offsets are below 50 µm, and the module indeed fits onto the cooling structure.

In summary, the DSM machine can now be used for serial production. The measurement results are understood, and the machine is easier to operate. The performance could also be improved. Investigations of the systematic uncertainties showed that a tilt of the module with respect to the camera could influence the measurement results. As a future improvement, a new mounting structure could be designed on which the modules can be mounted together with the structure in which they are carried in during assembly. This would save time as the modules are screwed to the supporting structure. It is expected that such a mounting structure would result in greater measurement uncertainties since the orientation of the sensor surface with respect to the cameras is likely to vary more with each mounting, reducing the reproducibility of the results. However, the statistical uncertainties of the current setup are so small that such a mounting structure could be considered.

Bibliography

[1] L. Evans and P. Bryant, *A Brief history and review of accelerators*, CERN (1992) .

[2] L. Evans and P. Bryant, *LHC Machine*, JINST **3** (2008) S08001.

[3] CMS Collaboration, *The CMS experiment at the CERN LHC*, JINST **3** (2008) S08004.

[4] G. Apollinari, O. Brüning, T. Nakamoto, and L. Rossi, *High Luminosity Large Hadron Collider (HL-LHC): Preliminary Design Report*, CERN-2015-005 (2015) .

[5] CMS Collaboration, *The Phase-2 Upgrade of the CMS Tracker*, Technical Report CERN-LHCC-2017-009, CMS-TDR-014 (2017) .

[6] CERN, *Large Hadron Collider restarts*. https://home.cern/news/news/accelerators/large-hadron-collider-restarts, visited on Juni 16, 2022.

[7] CERN, *The CERN accelerator complex*. https://home.cern/science/accelerators/accelerator-complex, visited on Juni 16, 2022.

[8] CMS Collaboration, *CMS Luminosity - Public Results*. https://twiki.cern.ch/twiki/bin/view/CMSPublic/LumiPublicResults, visited on June 16, 2022.

[9] I. B. Alonso et al., *High-Luminosity Large Hadron Collider (HL-LHC): Technical design report*, Technical Report CERN-2017-007-M (2020) .

[10] CMS Collaboration, *Observation of a new boson at a mass of 125 GeV with the CMS experiment at the LHC*, Physics Letters B **716** (2012) 30–61.

[11] CMS Collaboration, *SketchUpCMS*. https://twiki.cern.ch/twiki/bin/view/CMSPublic/SketchUpCMS, visited on June 17, 2022.

[12] W. Adam et al., *The CMS Phase-1 Pixel Detector Upgrade*, JINST **16** (2021) P02027.

[13] C. Collaboration, *Description and performance of track and primary-vertex reconstruction with the CMS tracker*, JINST **9** (2014) P10009.

[14] CMS Collaboration, *Performance of the CMS muon trigger system in proton-proton collisions at* $\sqrt{s} = 13\,TeV$, JINST **16** (2021) P07001.

[15] PETTL Collaboration, *Enabling Technologies for Silicon Microstrip Tracking Detectors at the HL-LHC*, DESY-16-072 (2016) .

[16] C. Käseberg, *Doppelseitige Vermessung von 2S-Modulen für das Upgrade des CMS-Spurdetektors*, Bachelor thesis, RWTH Aachen University (2017) .

[17] IDS Imaging, *UI-3250CP-rev-2*. https://de.ids-imaging.com/store/ui-3250cp-rev-2.html, visited on June 19, 2022.

[18] Mitutoyo, *M Plan Apo 10X*. https://shop.mitutoyo.de/web/mitutoyo/de_DE/mitutoyo/$catalogue/mitutoyoData/PR/378-803-3/datasheet.xhtml, visited on June 19, 2022.

[19] Aerotech, *Miniature Mechanical-Bearing, Screw-Driven Linear Stage MPS75SL(E)*. https://de.aerotech.com/wp-content/uploads/2020/10/MPS75SLE-Datasheet-11.2021-Revised.pdf, visited on June 19, 2022.

[20] ASI Imaging, *MS-8000 XY Automated Stage*. https://www.asiimaging.com/downloads/datasheets/MS-8000-Datasheet-Web.pdf, visited on June 19, 2022.

[21] ASI Imaging, *MS-2000-WK Multi-Axis Stage Controller*. https://www.asiimaging.com/downloads/datasheets/MS-2000-WK-Datasheet-Web.pdf, visited on June 19, 2022.

[22] Aerotech, *APR Hardware Manual*. https://www.aerotech.com/wp-content/uploads/2020/10/APR.pdf, visited on June 19, 2022.

[23] Aerotech, *Ensemble MP Hardware Manual*. https://www.aerotech.com/wp-content/uploads/2020/09/Ensemble-MP.pdf, visited on June 19, 2022.

[24] Sony, *Dualshock 4 Wireless-Controller Bedinungsanleitung*. https://www.playstation.com/content/dam/global_pdc/de/corporate/support/manuals/accessories/ps4-accessories/dualshock4-wireless-controller-cuh-zct2/CUH-ZCT2_DS4$de.pdf, visited on June 20, 2022.

[25] J. Canny, *A Computational Approach to Edge Detection*, IEEE Transactions on Pattern Analysis and Machine Intelligence **8** (1986) 679–698.

[26] R. O. Duda and P. E. Hart, *Use of the Hough transformation to detect lines and curves in pictures*, Communications of the ACM **15** (1972) 11–15.

[27] N. Röwert, *Assembly Studies of 2S-Module Prototypes for the CMS Phase-II Upgrade at LHC*, Bachelor thesis, RWTH Aachen University (2016) .

[28] Armacell, *AF/ArmaFlex*. https://local.armacell.com/de/armacell-deutschland/produkte/afarmaflex/, visited on July 31, 2022.

[29] Honeywell, *HIH-4000 Series Humidity Sensors*. https://www.tme.eu/Document/e6db3bab38139fc9aad882160ef7c62e/HIH-4000.pdf, visited on July 31, 2022.

[30] Keithley, *Model 2700 Multimeter/Switch System User's Manual*. https://download.tek.com/manual/2700-900-01K_Feb_2016.pdf, visited on July 31, 2022.

Danksagung

Hiermit bedanke ich mich zuerst bei Herrn Professor Feld für die Bereitstellung dieser Arbeit trotz anfänglicher erschwerter Corona Bedingungen. Das äußert konstruktive Feedback jede Woche hat maßgeblich zum Fortschritt der Arbeit beigetragen.
Außerdem danke ich Herrn Professor Pooth für die Übernahme der Zweitkorrektur.

Besonders danken möchte ich Martin Lipinski, der mein Hauptansprechpartner während der Arbeit war. Er konnte mir bei Fragen aller Art weiterhelfen. Außerdem bedanke ich mich für die Korrektur des Großteils dieser Arbeit. Nicht weniger bedanken möchte ich mich bei Katja Klein und Nicolas Röwert die ich ebenfalls immer ein offenes Ohr für mich hatten. Katja danke ich besonders für die Übernahme der Korrektur die nicht von Martin erledigt werden konnte. Nico danke ich speziell für das Einführen in das Setup und die Hilfe in spezielleren Fragen zur DSM.
Ich bedanke mich außerdem bei Clara Ebisch, für die überaus schnelle Herstellung der Anschlüsse für den Wärmetauscher.

Allgemein möchte ich mich auch bei dem gesamten Institut für die stets hilfsbereite Art jedes Mitarbeiters und das generell angenehme Arbeitsklima bedanken, in dem es mir viel Spaß gemacht hat diese Arbeit zu bestreiten.

Zu guter Letzt möchte ich mich bei meiner Freundin bedanken, die es immer geschafft hat mich aufzubauen, wenn es mal nicht so gut lief.